CHAPTER 13

Constrained Grain Boundary Diffusion in Thin Copper Films

Markus J. Buehler, T. John Balk, Eduard Arzt, Huajian Gao

Max Planck Institute for Metals Research, Stuttgart, Germany

CONTENTS

1. INTRODUCTION

Materials in small dimensions have become an increasingly important topic of research in the last decade. Changes in material behavior resulting from the effects of surfaces, interfaces, and constraints are still not completely understood. The focus of this chapter is on the mechanical properties of ultrathin submicron copper films on substrates. In such materials, important effects on the film surface and grain boundaries occur, and the constraint of the film–substrate interface can govern the mechanical behavior.

Polycrystalline thin metal films, shown schematically in Fig. 1, are frequently deposited on substrate materials to build complex microelectronic devices and are a relevant example of materials in small dimensions. In many applications and during the manufacturing process, thin films are subjected to stresses arising from thermal mismatch between the film material and the substrate. This can have a significant effect on the production yield as well as on the performance and reliability of devices in service. In past years, an ever-increasing trend toward miniaturization in technology has been observed, stimulating a growing interest in investigating the deformation behavior of ultrathin films with film thicknesses well below 1μm.

Different inelastic deformation mechanisms operate to relax the internal and external stresses on a thin film. Experiments have shown that for films of thicknesses between approximately 2 and 0.5 μm, the flow stress increases in inverse proportion to the film thickness (see, for example, Refs. [1–3]). This has been attributed to dislocation channeling through the film [4–6], where a moving threading dislocation leaves behind an interfacial segment. The relative energetic effort to generate these interfacial dislocations increases with decreasing film thickness, which explains the higher strength of thinner films. This model, however, could not completely explain the high strength of the thin films that was found in experiments [1]. More recent theoretical and experimental work [7–11] indicates that the strength of thin metal films often results from a lack of active dislocation sources rather than from the energetic effort associated with dislocation motion.
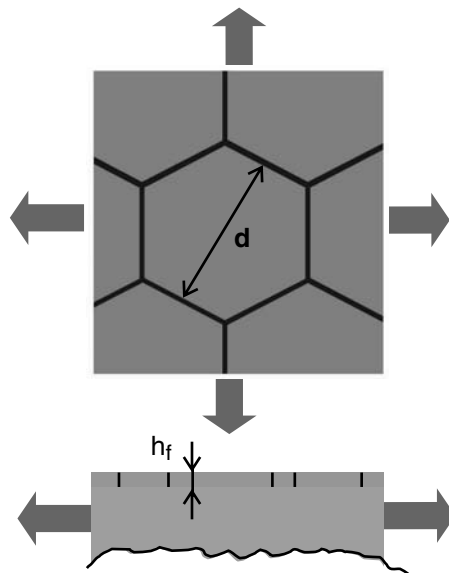

Figure 1. A polycrystalline thin film constrained by a substrate. The thin film is subject to biaxial loading as a result of thermal mismatch of film and substrate material.

The regime in which plastic relaxation is limited by dislocation nucleation and carried by the glide of threading dislocations reaches down to film thicknesses of about $h_f \approx 400$ nm. For yet-thinner films, experiments have revealed a film-thickness-independent flow stress [7]. *In-situ* transmission electron microscopy observations of the deformation of such ultrathin films reveal dislocation motion parallel to the film–substrate interface [7, 8]. This glide mechanism is unexpected, because in the global biaxial stress field, there is no resolved shear stress on parallel glide planes, indicating that there must be a mechanism involving long-range internal stresses that vary slowly on the length scale of the film thickness. For sufficiently thin films, these internal stresses have a pronounced effect on the mechanical behavior. Constrained diffusional creep [12] has provided what is so far the only feasible mechanism for such internal stresses to cause nucleation of dislocations on glide planes parallel to the surface.

This chapter contains three main parts. The first part reviews continuum mechanics modeling of constrained diffusional creep. The second part contains the results of molecular dynamics simulations of diffusional creep and plasticity in polycrystalline thin films. In the third part, we discuss relevant experimental results. Finally, we summarize all the results to develop a deformation mechanism map for ultrathin films on substrates.

2. CONTINUUM MODELING

The continuum model of constrained diffusional creep was developed by Gao and coworkers [12]. Diffusion can have a fundamentally different nature in thin films than in bulk materials. The constraint imposed by the strong bonding between film and substrate implies that no sliding can occur at the film–substrate interface. In contrast to previously proposed models of diffusion in thin films [13], the constraint of no sliding at the film–substrate interface renders diffusion in thin films an inherently transient phenomenon [12]. Therefore, steady-state solutions frequently used to describe grain boundary diffusion may not be applied. An additional constraint is that material transport cannot proceed in the substrate, and diffusion must therefore stop at the film–substrate interface. It was shown by Gao and coworkers [12] that constrained grain boundary diffusion leads to a new material defect, referred to as the grain boundary diffusion wedge.

Figure 2 illustrates the basic mechanism of constrained diffusional creep [12] in three stages. In stage 1, material is transported from the surface into the grain boundary. In stage 2, mass transport leads to the formation of a diffusion wedge, as more and more material flows into and accumulates in the grain boundary. The continuum model predicts that the traction along the grain boundary diffusion wedge becomes fully relaxed and cracklike on the scale of a characteristic time τ. This leads to extraordinarily large resolved shear stresses on glide planes that are parallel and close to the film–substrate interface, and that scan cause emission of parallel glide dislocations in the last stage. Although the resolved shear stresses on the parallel glide planes induced by a diffusion wedge are similar to those generated by a crack, differences in the dislocation nucleation process may arise.

This section is briefly outlined as follows. We discuss the continuum mechanics model of constrained diffusional creep for different cases, including the homogeneous case, bimaterial interface, and coupled surface and grain boundary diffusion. We also present an extension of the continuum model to include a threshold stress for diffusion. Finally, we discuss a model of the critical condition for initiation of diffusion and a model for parallel glide dislocation nucleation from the diffusion wedge in the spirit of a model by Rice and Thomson for dislocation nucleation at crack tips [14].

2.1. Basics of the Continuum Modeling

In the continuum model, diffusion is treated as a dislocation climb in the grain boundary. The basis for this decision is the solution for the normal traction σ_{xx} along the grain boundary resulting from the insertion of a single dislocation (material layer of thickness b) along $(0, \zeta)$ (corresponding to a climb edge dislocation). The coordinate system for the problem is depicted in Fig. 3. The solution for a single edge dislocation near a surface is used as the
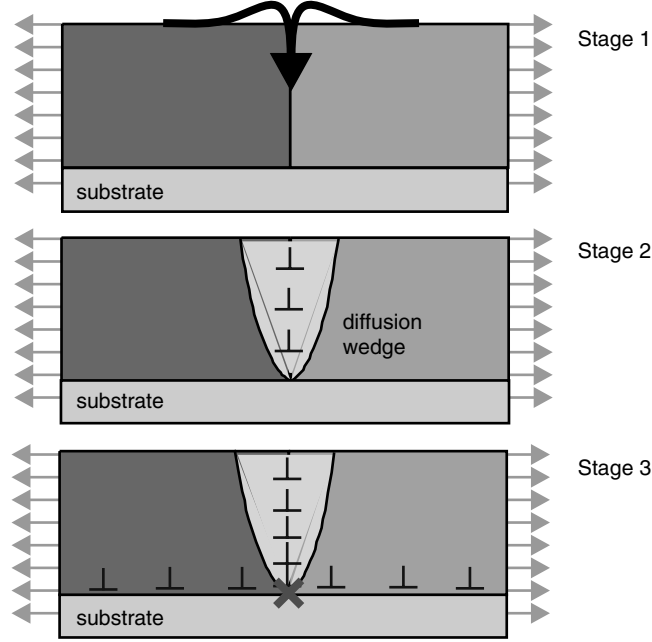
Figure 2. Mechanism of constrained diffusional creep. Material is transported from the surface into the grain boundary, leading to the formation of a diffusion wedge as material accumulates in the grain boundary. The diffusion wedge can be modeled as a pile-up of climb edge dislocations near the film–substrate interface, causing a cracklike singular stress concentration near the root of the grain boundary.

Green's function to construct a solution with infinitesimal Volterra edge dislocations [15–17]. The traction at position ζ resulting from a dislocation at ξ is

$$\sigma_{xx}(\zeta, \xi) = \frac{Eb}{4\pi(1 - \nu^2)} K(\zeta, \xi) \tag{1}$$

where

$$K(\zeta, \xi) = \frac{1}{\zeta - \xi} - \frac{1}{\zeta + \xi} - \frac{2\zeta(\zeta - \xi)}{(\zeta + \xi)^3} \tag{2}$$

is the Cauchy kernel function for this particular problem, with E denoting Young's modulus and ν Poisson's ratio. For an arbitrary opening function $2u(\zeta)$ in a film with thickness h_f, the stress along the grain boundary is given by

$$\sigma_{xx}(\zeta, t) = \sigma_0 - \frac{E}{2\pi(1 - \nu^2)} \int_0^{h_\mathrm{f}} S(\zeta, \xi) \frac{\partial u(\xi, t)}{\partial \xi} \, d\xi \tag{3}$$
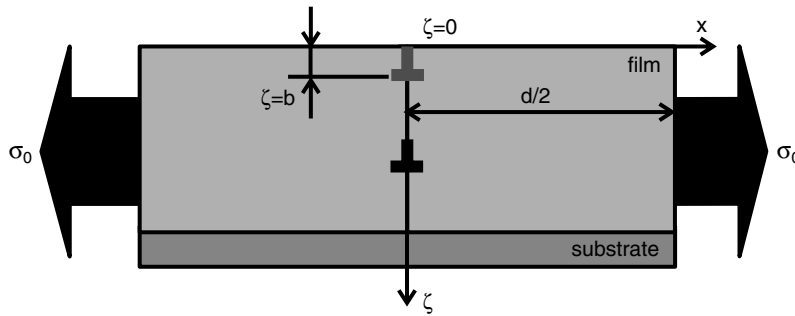

Figure 3. Coordinate system for the continuum mechanics analysis. The schematic shows climb edge dislocations in the grain boundary of a thin film on substrate.

where σ_0 is the stress in the absence of diffusion and $S(\zeta, \xi)$ is a Green's function kernel for the continuous dislocation problem (Cauchy kernel). For a dislocation near a free surface, $S(\zeta, \xi) = K(\zeta, \xi)$. The kernel function $S(\zeta, \xi)$ can also be established for a dislocation near a bimaterial interface [12, 18] or for periodic wedges [12]. The calculations in this chapter are mostly for an elastic film on a rigid substrate, although we do not give the Green's function kernel explicitly here.

The chemical potential relative to the free surface (with atomic volume $\Omega = a_0^3/4$ in face-centered cubic crystals where a_0 is the lattice parameter) is given by

$$\mu(\zeta, t) = \mu_0 - \sigma_{xx}(\zeta, t)\Omega \tag{4}$$

where μ_0 is an arbitrary reference constant. The corresponding atomic flux per unit thickness in the boundary is

$$j(\zeta, t) = -\frac{\delta_{gb}D_{gb}}{kT}\frac{\partial\mu(\zeta, t)}{\partial\zeta} = \frac{\delta_{gb}D_{gb}}{kT}\frac{\partial\sigma_{xx}(\zeta, t)}{\partial\zeta} \tag{5}$$

where k is the Boltzmann constant and T the absolute temperature. The parameter $\delta_{gb}D_{gb}$ denotes temperature-dependent grain boundary diffusivity. Equations (4) and (5) are coupled via mass conservation, as the flux divergence is related to the displacement rate through

$$2\frac{\partial u}{\partial t} = -\Omega\frac{\partial j(\zeta, t)}{\partial\zeta} \tag{6}$$

which can be combined with Eq. (5) as

$$\frac{\partial u}{\partial t} = -\frac{\delta_{gb}D_{gb}\Omega}{2kT}\frac{\partial^2\sigma_{xx}(\zeta, t)}{\partial\zeta^2} \tag{7}$$

The derivative of $\sigma_{xx}(\zeta, t)$ with respect to time is given by

$$\frac{\partial\sigma_{xx}(\zeta, t)}{\partial t} = -\frac{E}{2\pi(1-\nu^2)}\int_0^{h_f} S(\zeta, \xi)\frac{\partial^2 u(\xi)}{\partial\xi\partial t}\,d\xi \tag{8}$$

and inserting Eq. (7) into Eq. (8) yields the main governing equation

$$\frac{\partial\sigma_{xx}(\zeta, t)}{\partial t} = \frac{E\delta_{gb}D_{gb}\Omega}{4\pi(1-\nu^2)kT}\int_0^{h_f} S(\zeta, \xi)\frac{\partial^3\sigma_{xx}(\xi, t)}{\partial\xi^3}\,d\xi \tag{9}$$

for the grain boundary traction. Boundary and initial conditions are given as follows: for the continuity of chemical potential near the free surface,

$$\sigma_{xx}(\zeta = 0, t) = 0 \tag{10}$$

and for no sliding and no diffusion at the interface,

$$\frac{\partial\sigma_{xx}}{\partial\zeta}(\zeta = h_f, t) = \frac{\partial^2\sigma_{xx}}{\partial\zeta^2}(\zeta = h_f, t) = 0 \tag{11}$$

Finally,

$$\sigma_{xx}(\zeta, t = 0) = \sigma_0 \tag{12}$$

sets the initial condition for the transient problem.

The problem given by Eq. (9) can be expressed by the method of separation of variables in the form of an expansion series

$$\sigma_{xx}(\zeta, t) = \sigma_0\sum_{n=1}^{\infty} c_n\exp(-\lambda_n t/\tau)f_n(\zeta/h_f) \tag{13}$$

where

$$\tau = \frac{4\pi(1 - \nu^2)kTh_{\mathrm{f}}^3}{ED_{\mathrm{gb}}\delta_{\mathrm{gb}}\Omega} \tag{14}$$

is a characteristic time and λ_n, f_n, and c_n denote the eigenvalues, eigenfunctions, and coefficients. The coefficients are determined from the initial condition at $t = 0$. It is important to note that $\tau \sim h_{\mathrm{f}}^3$, similar to the classical Coble creep equation [19]. To solve the equations numerically, the problem is transformed into a standard Cauchy-type singular equation for f_n''' [12]. The Gauss–Chebyshev quadrature developed by Erdogan et al. [20, 21] can be used to solve such equations. The opening displacement $u(z, t)$ is given by

$$u(\zeta, t) = -\frac{2\pi(1 - \nu^2)h_{\mathrm{f}}\sigma_0}{E} \sum_{n=1}^{\infty} c_n\lambda_n^{-1}\left(1 - \exp\left(-\lambda_n t/\tau\right)\right)f_n''(\zeta/h_{\mathrm{f}}) \tag{15}$$

The solution procedure can be summarized in the following steps: first, find eigenvalues and eigenfunctions; second, find the coefficients c_n, and third, calculate the traction and displacement from Eqs. (13) and (15).

The dislocations "stored" in the grain boundary represent additional material in the boundary. With respect to the lattice distortion around the diffusion wedge, the dislocations in the grain boundary exemplify a type of geometrically necessary dislocation [22] that causes nonuniform plastic deformation in the thin film. The eigenvalues measure the rate of decay of each eigenmode. The results showed that the higher eigenmodes decay much faster than the first eigenmode, so the diffusion process is dominated by the first eigenmode [12].

Figures 4, 5, and 6 show several numerical examples. Figure 4 shows the stress intensity factor normalized by the corresponding value for a crack versus the reduced time $t^* = t/\tau$ for identical elastic properties of substrate and film material (homogeneous case), rigid substrate (copper film and rigid substrate), and soft substrate (aluminum film and epoxy substrate). Table 1 summarizes the material parameters used for the calculation. In the table, $\mu_{\mathrm{film}}/\mu_{\mathrm{subs}}$ is the ratio of the shear moduli.

Figure 5 shows the opening displacement along the grain boundary for several instants in time for the case of soft film on rigid substrate, and Fig. 6 shows the traction along the boundary for various instants in time. These examples illustrate that in the long time limit $t \to \infty$, the solution approaches the displacement profile of a crack.

For constrained diffusional creep to proceed, both grain boundary diffusion and surface diffusion need to be active. In the original paper on constrained diffusional creep [12],
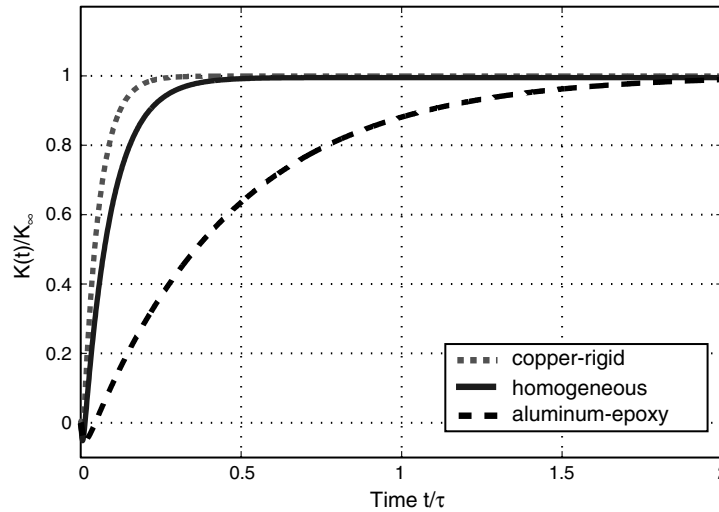

Figure 4. Development of stress intensity factor over time for the cases of an elastically homogeneous film on substrate, a rigid substrate, and a soft substrate. The convergence to the stress intensity factor of a crack is fastest for a rigid substrate and slowest for a soft substrate.
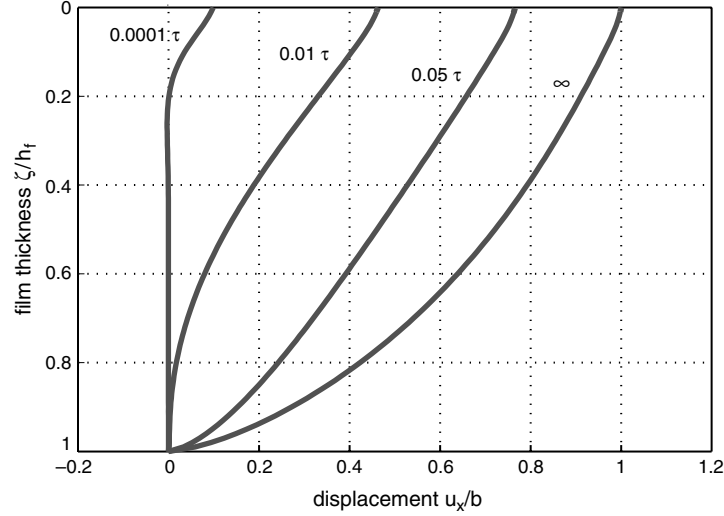
Figure 5. Development of grain boundary opening u_x normalized by a Burgers vector over time, in the case of a copper film on a rigid substrate. The loading σ_0 is chosen such that the opening displacement at the film surface ($\zeta = 0$) at $t \to \infty$ is one Burgers vector.

surface diffusion was assumed to be infinitely fast relative to grain boundary diffusion. This implies that grain boundary diffusion is the rate-limiting factor. To account for cases when surface diffusion is slower than grain boundary diffusion, or for cases when surface and grain boundary diffusion occur on comparable timescales, the model was extended in a later publication to also include the effect of surface diffusion [18]. We now briefly review this model.

The atomic flux on a free surface may be expressed as

$$j_s(s, t) = \frac{\delta_s D_s}{kT} \frac{\partial \mu_s}{\partial s} \tag{16}$$

Here $\partial \mu_s / \partial s$ refers to the gradient in chemical potential along the free surface, and $\delta_s D_s$ is the temperature-dependent coefficient of surface diffusion. The chemical potential of an
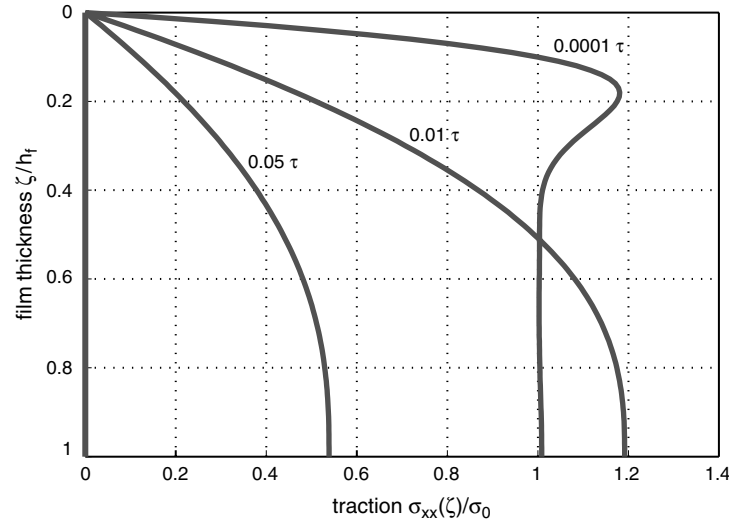

Figure 6. Development of grain boundary traction σ_{xx}/σ_0 over time for the case of a copper film on a rigid substrate. The grain boundary traction approaches σ_0 when $t \to 0$, and the grain boundary traction relaxes to zero when $t \to \infty$.

Table 1. Material parameters for calculation of stress intensity factor over the reduced time.

	ν_{film}	ν_{subs}	$\mu_{\text{film}}/\mu_{\text{subs}}$
Cu/rigid	0.32	—	0
Al/epoxy	0.3	0.35	23.08
isotropic	—	—	1

atom at surface is

$$\mu_s = \mu_0 - \Omega \gamma_s \kappa(s, t) \tag{17}$$

where the contribution from elastic energy is neglected, following Rice and Chuang [23]. Here, γ_s is the surface energy and $\kappa(s, t)$ is the local surface curvature. Assuming that the surface slope is small, the governing equation for the surface evolution can be expressed by Mullins' equation [24]:

$$\dot{y}(x, t) = -\frac{\delta_s D_s \gamma_s \Omega}{kT} y''''(x, t) \tag{18}$$

where y measures the deviation of the surface relative to the flat surface and $\dot{y}$ is the time derivative of y. The boundary and initial conditions for the present problem are given as

$$y'(0, t) = \cos(\Psi) \qquad y'(d/2, t) = y'''(d/2, t) = 0 \qquad \text{and} \qquad y(x, 0) = 0 \tag{19}$$

where d is the grain size in the x-direction, with $d/2$ referring to the midpoint of the grain, as shown in Fig. 3. The parameter

$$\Psi = \cos^{-1}\left(\frac{\gamma_{\text{gb}}}{2\gamma_s}\right) \tag{20}$$

is the angle of grain boundary groove to be calculated from γ_s and the grain boundary energy γ_{gb}.

Solving the fully coupled grain boundary and surface diffusion problem is rather difficult. In [18] it was proposed that the two problems be solved separately by assuming that the surface retains a small slope such that the kernel function $S(z, \zeta)$ remains invariant during surface diffusion. The link between the two governing Eqs. (9) and (18) is the continuity of chemical potential at the intersection of the grain boundary and the free surface

$$\sigma_{\text{gb}}(0, t) = \gamma_s \kappa(0, t) = \gamma_s y''(0, t) \tag{21}$$

and that of atomic flux

$$\delta_{\text{gb}} D_{\text{gb}} \sigma'_{\text{gb}}(0, t) = -2\delta_s D_s \gamma_s y'''(0, t) \tag{22}$$

For the case of infinitely fast grain boundary diffusion, a characteristic time for stress decay can be defined as

$$\tau_s = \frac{kTh_f^3(1 - \nu^2)}{E\delta_s D_s \Omega} \tag{23}$$

Note that τ_s is defined 4π larger than that adopted in Ref. [18].

In Ref. [18], solutions are reported for different ratios of the rate of surface diffusion relative to grain boundary diffusion and vice versa. The ratio $\Delta = \tau_{\text{gb}}/\tau_s$ determines the relative importance of grain boundary to surface diffusion, where τ_{gb} is equal to τ defined in Eq. (14). For all values of Δ, constrained grain boundary diffusion leads to exponential relaxation of grain boundary traction, and the relaxation results in a singular stress field at the root of the grain boundary. Another important finding was that in all cases (even if grain boundary diffusion is comparable in rate to surface diffusion), the characteristic timescales

with the cube of the film thickness $\tau \sim h_{\mathrm{f}}^3$. The main result reported in Ref. [18] is that an effective diffusivity could be defined according to an empirical mixing rule

$$\tau_{\mathrm{eff}} = \frac{4\pi \mathrm{k} T h_{\mathrm{f}}^3 (1 - \nu^2)}{\delta_{\mathrm{eff}} D_{\mathrm{eff}} \Omega E} \tag{24}$$

where

$$\delta_{\mathrm{eff}} D_{\mathrm{eff}} = \delta_{\mathrm{gb}} D_{\mathrm{gb}} \frac{\Delta}{\Delta + \alpha} \tag{25}$$

and α is a constant to be determined by matching the relaxation behavior for different values of Δ. In Ref. [18], α was determined to be around 1/3.

2.2. Average Stress and Thermal Cycling Experiments

Weiss and coworkers [25] extended the continuum model based on a convolution procedure to model their thermal cycling experiments. The average stress in the film is calculated and compared to direct measurement in the laboratory.

Because the averaged grain boundary traction follows an exponential time decay [12], the average stress in the grain boundary can be approximated as

$$\hat{\sigma}_{\mathrm{gb}}(t) = \sigma_0 \exp\left(-\lambda_0 t / \tau\right) \tag{26}$$

with a geometry-dependent constant

$$\lambda_0 = 8.10 + 30.65 h_{\mathrm{f}} / d \tag{27}$$

Here, d is the grain size, and σ_0 is the reference stress in the absence of diffusion, as discussed in Section 2.1. Equation (27) is an empirical formula and is valid for $0.2 \le h_{\mathrm{f}}/d \le 10$. The loading rate of applied stress with respect to temperature is given by

$$\frac{d\sigma_0}{dT} = -\Delta\alpha M_{\mathrm{f}} \tag{28}$$

Then, with $\dot{T}$ as the time derivative of the temperature (heating or cooling rate),

$$\hat{\sigma}_{\mathrm{gb}}(t) = \sigma_0 \exp\left[-\lambda \int_{T_{\mathrm{start}}}^{T} \frac{d\zeta}{\dot{T}\tau(\zeta)}\right] - M_{\mathrm{f}}\Delta\dot{T} \int_{T_{\mathrm{start}}}^{T} \exp\left[-\frac{\lambda}{\dot{T}}\left(\int_{\zeta}^{T} \frac{d\xi}{\tau(\xi)}\right)\right] \frac{1}{\dot{T}} d\zeta \tag{29}$$

where T is the temperature at time t, and T_{start} is the starting temperature. The average stress σ in the film is related to σ_0 and $\hat{\sigma}_{\mathrm{gb}}$ as

$$\sigma = \sigma_0 - (\sigma_0 - \hat{\sigma}_{\mathrm{gb}})\Theta \tag{30}$$

where

$$\Theta = \frac{4h_{\mathrm{f}}}{d} \tanh\left(\frac{d}{4h_{\mathrm{f}}}\right) \tag{31}$$

Equation (30) was obtained from an analysis of a periodic array of cracks in a thin elastic film analyzed by Xia and Hutchinson [26]. For a given experimentally measured stress σ, the average stress in the grain boundary $\hat{\sigma}_{\mathrm{gb}}$ is given by

$$\hat{\sigma}_{\mathrm{gb}} = \frac{1}{\Theta}(\sigma - \sigma_0) + \sigma_0 \tag{32}$$

The average film stress depends on the ratio of grain size to film thickness.

With full grain boundary relaxation and no further diffusion, the average stress follows a thermoelastic line with a reduced slope of

$$\frac{d\sigma}{dT} = -\Delta\alpha M_{\mathrm{f}} (1 - \Theta) \tag{33}$$

2.3. Single Edge Dislocations in Nanoscale Thin Films

Mass transport from the film surface into the grain boundary was modeled as a climb of infinitesimal edge dislocations [12, 18]. However, diffusion into the grain boundary must proceed with at least one atomic column. At the nanoscale, dislocation climb in the grain boundary becomes more of a discrete process. Grain boundary diffusion requires insertion of discrete climb dislocations into the grain boundary, a fact that has not been accounted for by the continuum model.

To investigate this effect, we consider a single edge dislocation climbing along a grain boundary in an elastic film of thickness h_f on a rigid substrate. The elastic solution of edge dislocations in such a film can be obtained using the methods described in Refs. [15, 27].

The geometry is shown in Fig. 3. A dislocation placed inside the film is subjected to image forces arising from the surface and the film–substrate interface. The image stress on a dislocation for different film thicknesses is shown in Fig. 7. Between the film surface and the film–substrate interface, the image force is found to attain a minimum value at $\zeta_{EQ} \approx 0.4 h_f$.

From the energetic point of view, a minimum critical stress is required to allow a single climb edge dislocation to exist in the grain boundary. The thicker the film, the smaller this critical stress. This analysis suggests that consideration of single, discrete dislocations could become very important for nanoscale thin films. For films around 5 nm in thickness, the minimum critical stress for one stable dislocation in the grain boundary approaches 1 GPa. The requirement that an edge dislocation in the film be in a stable configuration could be regarded as a necessary condition for the initiation of constrained grain boundary diffusion.

2.4. Initiation Condition for Diffusion

Considerations similar to those in the previous section were employed to determine conditions under which diffusion could initiate. In Ref. [28], a criterion for the initiation of grain boundary diffusion is proposed, following the spirit of the Rice–Thomson model [14]. It is postulated that the condition for initiation of diffusion is a local criterion, independent of the film thickness.

The main assumption is that grain boundary diffusion is initiated when a test climb dislocation near the surface is spontaneously inserted into the grain boundary. Considering the force balance on the critical configuration of an edge dislocation located one Burgers vector away from the free surface, as shown in Fig. 3, a critical lateral stress

$$\sigma_0^{crit} > \frac{E}{8\pi(1-\nu^2)} \tag{34}$$
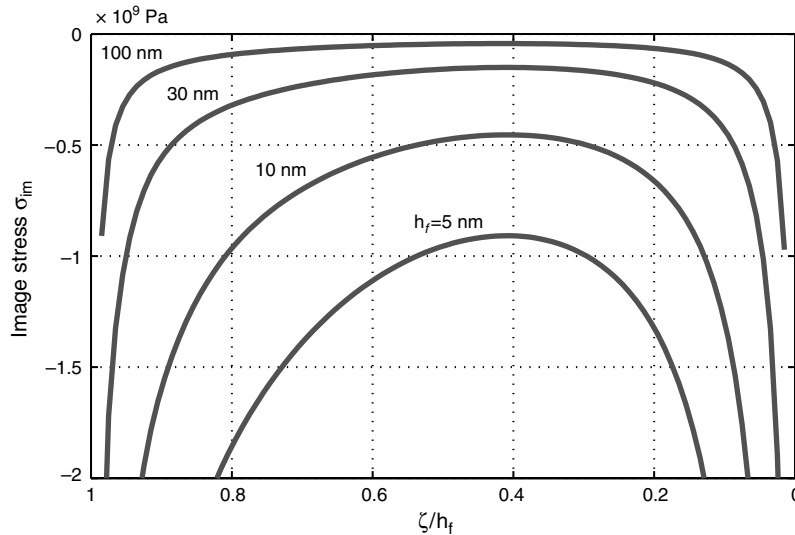

Figure 7. Image stress on a single edge dislocation in a thin film for different film thicknesses ranging from 5 to 100 nm.

can be defined for spontaneous insertion of the test dislocation into the grain boundary. Note that E should be interpreted here as the local modulus of the grain boundary near the surface, which could be much smaller than the bulk modulus. This result implies that a critical stress independent of the film thickness is required for the onset of grain boundary diffusion.

2.5. Nucleation Criterion for Parallel Glide Dislocations

A criterion based on a critical stress intensity factor K^{PG} was proposed for the nucleation of parallel glide dislocations at grain boundary diffusion wedges [28].

The stress intensity factor at the root of a crack or diffusion wedge is defined as

$$K = \lim_{\zeta \to h_f} \left\{ [2\pi(\zeta - h_f)]^s \, \sigma_{xx}(0, \zeta) \right\} \tag{35}$$

where s refers to the stress singularity exponent that can be determined from Ref. [29].

$$\cos(s\pi) - 2\frac{\alpha - \beta}{1 - \beta}(1 - s)^2 + \frac{\alpha - \beta^2}{1 - \beta^2} = 0 \tag{36}$$

The parameters α and β are Dundur's parameters, which measure the elastic mismatch of film and substrate material.

It is assumed that the diffusion wedge is located close to a rigid substrate, and the corresponding Dundur's parameters for this case are $\alpha = -1$ and $\beta = -0.2647$. The singularity exponent is found to be $s \approx 0.31$ for the material combination considered in our simulations (compared to $s = 0.5$ in the case of a homogeneous material). Close to the bimaterial interface, we calculate the stress intensity factor

$$K = A \times \lim_{\zeta \to h_f} \left(\frac{\partial u_x(\zeta)}{\partial \zeta}(1 - (\zeta/h_f)^2)^s \right) (\pi h_f)^s \tag{37}$$

where

$$A = \frac{E}{1 - \nu^2} \frac{(1 - \alpha)}{4\sin(\pi s)} \left(\frac{3 - 2s}{1 + \beta} - \frac{1 - 2s}{1 - \beta} \right) \tag{38}$$

The stress intensity factor provides an important link between the atomistic results and continuum mechanics. To calculate the stress intensity factor from atomistic data, the atomic displacements of the lattice close to the diffusion wedge are calculated and the stress intensity factor is then determined using Eq. (37).

A common approach to study the nucleation of dislocations from defects is to balance the forces on a test emergent dislocation [14]. The force on dislocations element is referred to as Peach–Koehler force, which can be written as $d\mathbf{F}_d = (\sigma \cdot \mathbf{b}) \times d\mathbf{l}$, where $d\mathbf{l}$ is the element length vector and σ is the local stress [16]. A dislocation is assumed to be in an equilibrium position when $F_d = 0$. Following the Rice-Thomson model [14], we consider the force balance on a probing dislocation in the vicinity of a dislocation source to define the nucleation criterion. The probing dislocation is usually subject to an image force attracting it toward the source, as well as a force resulting from applied stress driving it away from the source. The image force dominates at small distances, and the driving force caused by applied stress dominates at large distances. There is thus a critical distance between the dislocation and the source at which the dislocation attains unstable equilibrium. Spontaneous nucleation of a dislocation can be assumed to occur when the unstable equilibrium position is within one Burgers vector of the source.

Nucleation of parallel glide dislocations from a crack in comparison to that from a diffusion wedge is shown in Fig. 8. The crack case is treated similarly as in Ref. [14], and the forces involved are F_c because of the crack tip stress field, F_{image} from the crack surface (image dislocation), and F_{step} because of the creation of a surface step, which is assumed to be negligible in comparison of F_{image}.

Close to a diffusion wedge, $F_{step} = 0$ because no surface step is involved, and a dipole must be created to nucleate a parallel glide dislocation from the wedge. This leads to a
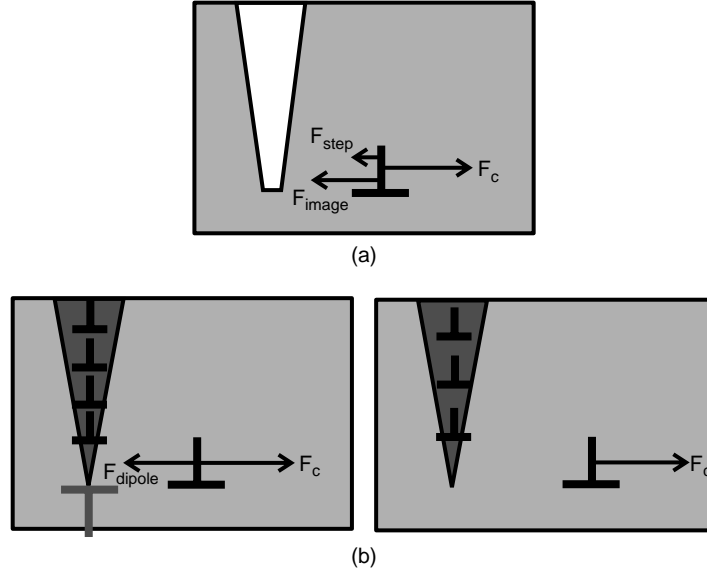
Figure 8. Force balance on a dislocation near (a) a crack (top) and (b) a diffusion wedge (bottom).

dipole interaction force F_{dipole}. The dipole consists of a pair of dislocations of opposite signs, one pinned at the source and the other trying to emerge and escape from the source. The pinned end of the dipole has the opposite sign of the climb dislocations in the diffusion wedge and can be annihilated via climb within the grain boundary. Such annihilation breaks the dipole free and eliminates the dipole interaction force so that the emergent end of the dipole moves away to complete the nucleation process. Therefore, it seems that there could be two possible scenarios for dislocation nucleation at a diffusion wedge. In the first scenario, the nucleation condition is controlled by a critical stress required to overcome the dipole interaction force. In the second scenario, the nucleation criterion is controlled by the kinetics of climb annihilation within the grain boundary, which breaks the dipole interaction by removing its pinned end and setting the other end free. The force balance on the dislocation is illustrated in Fig. 8 for two different, subsequent instants in time.

We assume that dislocation nucleation at a diffusion wedge is stress controlled (rather than kinetics controlled), and the first scenario of dislocation nucleation described above is adopted. This assumption has been verified by recent molecular dynamics simulations [28]. With this assumption, it is possible to define a nucleation criterion in terms of a critical stress intensity factor. We illustrate the critical condition for dislocation nucleation in Fig. 9. A force balance on a dislocation near a crack tip at a rigid bimaterial interface leads to the critical stress intensity factor for dislocation nucleation from a crack

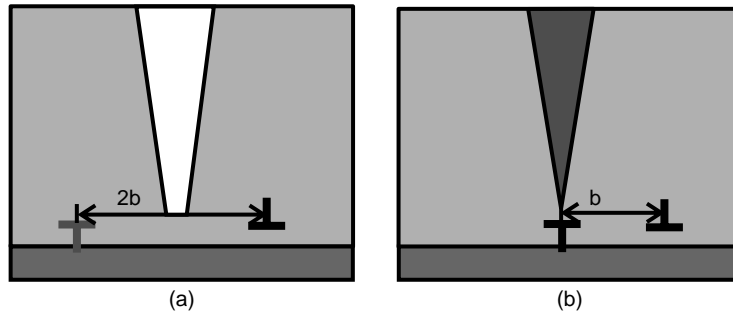$$K_{cr}^{PG} = \frac{E(2\pi b)^s}{8\pi(1-\nu^2)} \tag{39}$$

Figure 9. Nucleation of parallel glide dislocations from (a) a crack and (b) a diffusion wedge.

In comparison, a balance of critical stress required to break the dipole interaction in front of a diffusion wedge yields a similar nucleation criterion

$$K_{\text{dw}}^{\text{PG}} = \frac{E(2\pi b)^s}{4\pi(1 - \nu^2)} \tag{40}$$

For copper with $b = 2.56$ Å, $E \approx 150$ GPa, and $\nu = 0.33$, typical values are $K_{\text{cr}}^{\text{PG}} \approx 12.5$ MPa $\times$ m^s and $K_{\text{dw}}^{\text{PG}} \approx 25$ MPa $\times$ m^s. We note a factor of 2 difference in the critical K-values, $K_{\text{dw}}^{\text{PG}}/K_{\text{cr}}^{\text{PG}} = 2$, for dislocation nucleation at a diffusion wedge and at a crack tip.

2.6. Constrained Grain Boundary Diffusion with Threshold Stress

In recent molecular dynamics and discrete dislocation simulations [28, 30, 31] of constrained diffusional creep in thin films, it has been shown that the stress does not relax to zero in the film. Also, a critical stress σ_0^{crit} is found to be necessary to initiate diffusion. In addition to the theoretical considerations (see Section 2.4), experimental results of stress–temperature plots during thermal cycling also indicate a threshold stress for diffusion [8]. In the following, we extend the continuum model to include a threshold stress.

Equation (9) is the governing equation for the problem of constrained diffusional creep. Assuming a threshold stress σ_t for grain boundary diffusion, the boundary conditions are now modified as

$$\sigma_{xx}(\zeta = 0, t) = \sigma_t \tag{41}$$

and

$$\frac{\partial \sigma_{xx}}{\partial \zeta}(\zeta = h_{\text{f}}, t) = \frac{\partial^2 \sigma_{xx}}{\partial \zeta^2}(\zeta = h_{\text{f}}, t) = 0 \tag{42}$$

The initial condition remains the same

$$\sigma_{xx}(\zeta, t = 0) = \sigma_0 \tag{43}$$

We consider the possibility that σ_t may be different under tension and compression. That is, no grain boundary diffusion can occur when

$$\sigma_t^- < \sigma_{xx}(0, t) < \sigma_t^+ \tag{44}$$

where $\sigma_{xx}(0, t)$ is the stress at the site of initiating climb edge dislocations near the entrance to the grain boundary.

Using superposition,

$$\sigma_{xx}(\zeta, t) = \sigma_t + \tilde{\sigma}(\zeta, t) \tag{45}$$

we obtain the governing equation for $\tilde{\sigma}(\zeta, t)$ as

$$\frac{\partial \tilde{\sigma}_{xx}(\zeta, t)}{\partial t} = \frac{E D_{\text{gb}} \delta_{\text{gb}} \Omega}{4\pi(1 - \nu^2)kT} \int_0^{h_{\text{f}}} S(\zeta, \xi) \frac{\partial^3 \tilde{\sigma}_{xx}(\xi, t)}{\partial \xi^3} d\xi \tag{46}$$

The boundary conditions are

$$\tilde{\sigma}_{xx}(\zeta = 0, t) = 0 \tag{47}$$

$$\frac{\partial \tilde{\sigma}_{xx}}{\partial \zeta}(\zeta = h_{\text{f}}, t) = \frac{\partial^2 \tilde{\sigma}_{xx}}{\partial \zeta^2}(\zeta = h_{\text{f}}, t) = 0 \tag{48}$$

and the initial condition is

$$\tilde{\sigma}_{xx}(\zeta, t = 0) = \sigma_0 - \sigma_t \tag{49}$$

These equations are identical to those of Ref. [12], except that the initial condition is effectively reduced. Therefore, we can simply use the previous solution [see Eq. (26)] to obtain the average stress along the grain boundary as

$$\hat{\sigma}_{\mathrm{gb}}(t) = (\sigma_0 - \sigma_t)\exp{(-\lambda_0 t/\tau)} + \sigma_t \tag{50}$$

Figure 10(a) shows a numerical example of the decay of the average stress in the film as given by Eq. (30) both with and without threshold stress. The parameter σ_t^+ is assumed to be 65 MPa. For comparison, experimental stress relaxation curves for 200- and 800-nm Cu films are presented in Fig. 10(b). The experimental results show that the film stress does not decay to zero but, instead, approaches a plateau value.

We can now generalize the convolution procedure described by Weiss et al. [25]

$$\frac{d\sigma_0}{dT} = -\Delta\alpha M_{\mathrm{f}} \tag{51}$$

Then,

$$\hat{\sigma}_{\mathrm{gb}}(t) = \sigma_t + \left(\sigma_0^{\mathrm{start}} - \sigma_t\right)\exp\left[-\lambda \int_{T_{\mathrm{start}}}^{T} \frac{d\zeta}{\dot{T}\tau(\zeta)}\right]$$

$$- M_{\mathrm{f}}\Delta\dot{T}\int_{T_{\mathrm{start}}}^{T}\exp\left[-\frac{\lambda}{\dot{T}}\left(\int_{\zeta}^{T}\frac{d\xi}{\tau(\xi)}\right)\right]\frac{1}{\dot{T}}\,d\zeta \tag{52}$$

The average stress in the film as measured in experiment is calculated from $\hat{\sigma}_{\mathrm{gb}}(t)$ by using Eq. (30).

2.7. Discussion and Summary of Continuum Modeling

We summarize the main results of the continuum modeling: first, the continuum model predicts an exponential decay of stress in the thin film with a characteristic time $\tau \sim h_{\mathrm{f}}^3$, similar to the classical Coble creep [19]. A new defect referred to as a "diffusion wedge" is built up by the pileup of edge dislocations in the grain boundary [12] on the order of the characteristic time τ. Second, the continuum model predicts that the deformation field near a diffusion wedge becomes cracklike on the order of the characteristic time τ [12, 18]. Third, for nanoscale thin films, the effect of discrete dislocations becomes important as the image stress on a single dislocation reaches several hundred MPa [32]. Fourth, treatment of atomic diffusion from a free surface into the grain boundary by the climb of discrete edge dislocations suggests a threshold stress for diffusion initiation independent of film thickness [28, 30, 32]. Finally, a condition for the nucleation of parallel glide dislocations from a
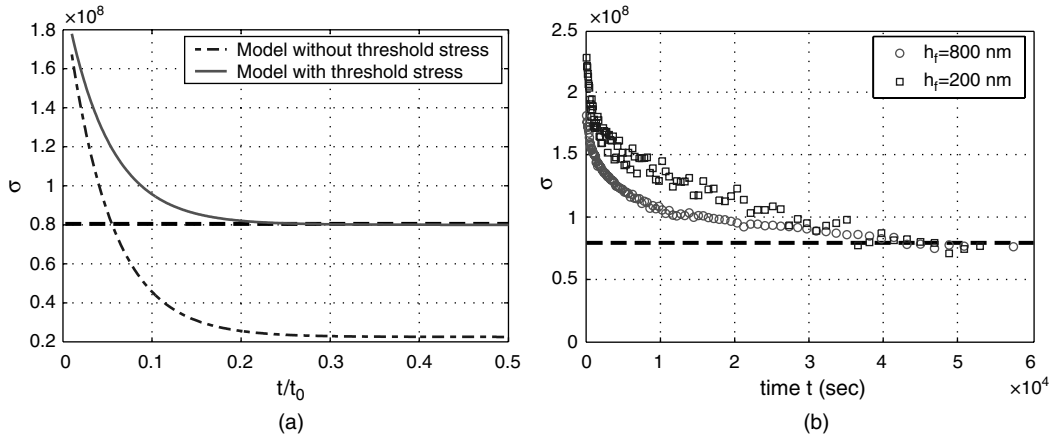

Figure 10. (a) Prediction of stress decay by the continuum model with and without threshold stress. (b) Experimental results of stress decay at 250°C for $h_{\mathrm{f}} = 200$ nm and $h_{\mathrm{f}} = 800$ nm.

grain boundary diffusion wedge has been derived based on the force balance on a probing dislocation, in the spirit of the Rice–Thomson model [32].

The continuum modeling provided key input toward the understanding of the plasticity of ultrathin films. However, some of the atomic aspects of diffusion could not be understood from the standpoint of continuum modeling alone. This lack of understanding motivated the development of atomistic models.

3. ATOMISTIC MODELING

Under the guidance of the continuum model [12, 18, 27], atomistic simulations have proven to be capable of providing a detailed description of how parallel glide dislocations are nucleated near a diffusion wedge. In the following sections we summarize the main results of recent molecular dynamics simulations of constrained grain boundary diffusion [28, 30, 32].

Large-scale atomistic modeling provides a helpful tool for investigating material phenomena from a fundamental perspective. The methodology of atomistic simulations together with their strengths and shortcomings are discussed in another chapter of this book [33].

3.1. Large-Scale Atomistic Simulations of Plasticity in Polycrystalline Thin Films

It was proposed that traction relaxation along grain boundaries in thin films significantly alters the mechanism of dislocation nucleation and motion [7, 12]. In a recent paper [30], the effect of grain boundary traction relaxation on the plasticity of polycrystalline thin films was investigated, with the focus being the dynamics of defect evolution in films both with and without traction relaxation.

The molecular dynamics simulations showed that the relaxation of grain boundary tractions changes the dislocation microstructure and triggers different stress relaxation mechanisms in thin films. Threading dislocations dominate when tractions along the grain boundaries are not relaxed, as shown in Fig. 11(a). If the grain boundary tractions are relaxed, parallel glide dislocations dominate, as in Fig. 11(b). Threading dislocations were found to be mostly complete dislocations, whereas a strong tendency to nucleate partial dislocations is seen in the case of parallel glide dislocations in the nanometer-sized grains. This is qualitatively consistent with the results of atomistic modeling the deformation of nanocrystalline materials [34, 35]. Twinning along parallel planes becomes an active deformation mechanism at high strain rates. Figure 12 shows that threading dislocations dominate
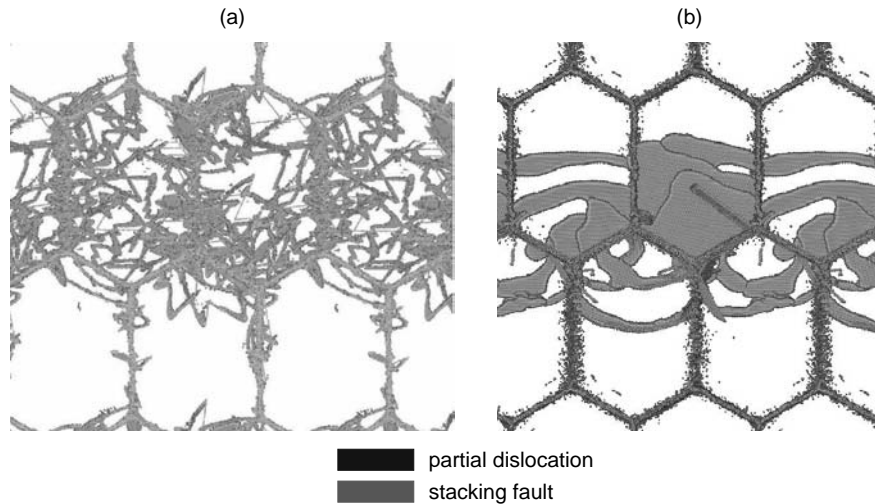

Figure 11. Plasticity in a polycrystalline thin film (a) without and (b) with grain boundary traction relaxation. When grain boundary tractions are not relaxed, threading dislocations dominate plasticity. In contrast, when the tractions are relaxed, parallel glide dislocations dominate. The plot shows dislocations as curved lines, and stacking faults as dark areas.
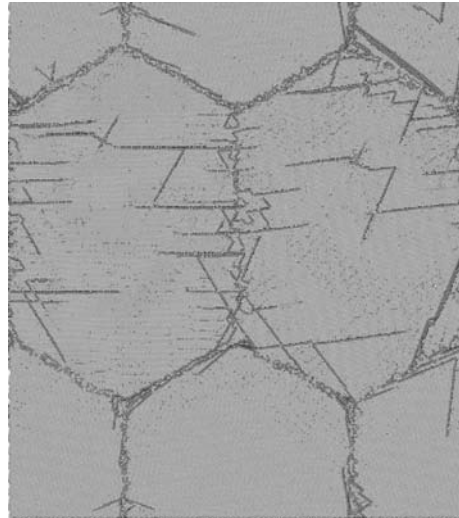
Figure 12. Plasticity in a polycrystalline thin film without grain boundary traction relaxation. The threading dislocations dominate. The plot shows a view on the surface, showing creation of surface steps as dark lines.

plasticity when grain boundary relaxation is shut down. Threading dislocations leave surface steps as they glide through the crystal.

Further studies in Ref. [30] focused on the influence of grain boundary structure on the nucleation of parallel glide dislocations.

A tricrystal model was considered with different types of grain boundaries, as shown in Fig. 13(a), to investigate the difference between low-energy (symbol A in the plot) and high-energy grain boundaries (symbol B in the plot). Low-energy grain boundaries are composed of an array of misfit grain boundary dislocations that serve as multiple nucleation sites for dislocations. It was observed that low-energy grain boundaries provide more fertile sources for threading dislocation nucleation. At such a boundary, dislocations are often observed to nucleate close to the misfit dislocations. This could be referred to as an intrinsic condition, as the structure of the grain boundary leads to local stress magnification at the misfit dislocations that serve as the source of parallel glide dislocations. Because it is possible that the incipient dislocations are nucleated on different glide planes, dislocation reactions may take place when several of them combine to form a single dislocation. The formation of jogs was observed in the dislocation line, generating trails of point defects that significantly hinder the motion of dislocations.

In the more homogeneous high-energy grain boundaries, there is inherently no preferred nucleation site, in which case triple junctions of grain boundaries serve as the nucleation
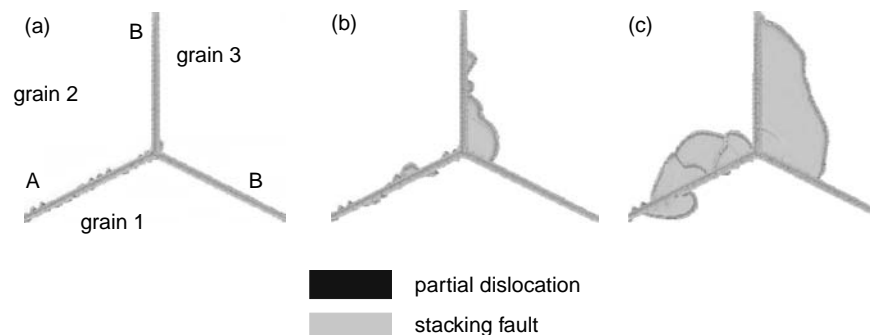

Figure 13. A temporal sequence of nucleation of parallel glide dislocations from grain boundaries in a triple junction model. Grain boundary type A refers to low-energy grain boundaries, and B corresponds to high-energy grain boundaries.

site. A temporal sequence of dislocation nucleation from a grain boundary triple junctions is shown in Fig. 13(a)–(c).

3.2. Atomistic Modeling of Diffusional Creep

Atomistic modeling of thin-film mechanics may become routine with the advent of massively parallel computers on time- and length-scales comparable with those usually attained in experimental investigations. Because of the time limitation of the classical molecular dynamics method (time intervals typically $<10^{-8}$ s), simulations of diffusional creep were performed at elevated temperatures to accelerate the dynamics of grain boundary diffusion [33].

The phenomenon of grain boundary diffusion wedge and the associated dislocation mechanisms persist at very high temperatures, making it possible to simulate this phenomenon using classical molecular dynamics [36, 37]. At elevated temperatures, grain boundary diffusion in a bulk material was recently successfully modeled [36], where grain sizes up to 15 nm were considered in a model system of palladium. Recent work [36, 38, 39] suggests that at elevated temperatures, the grain boundary structure of metals may transform into a liquid-like structure with a width up to several nanometers, which was referred to as a "glassy phase." Glassy phases in grain boundaries were found in copper at homologous temperatures as low as $T_h \approx 0.4$ [39, 40]. Experimental evidence for glassy intergranular phases was discussed in Ref. [41]. Such phase transformation at the grain boundary plays a significant role in the plastic properties at elevated temperatures because each different grain boundary structure has significant influence on the diffusion [38, 39].

To investigate creep behavior, the sample was loaded according to a prescribed strain field. An important result of the simulations was that diffusion cannot relax stresses in such thin films completely. These observations are qualitatively consistent with the predictions of Eq. (34) and are in agreement with experimental results.

The snapshots in Fig. 14 show how the displacement changes as material diffuses into the grain boundary. The horizontal coordinates have been stretched by a factor of 10 in x-direction to make the crystal lines clearly visible; that is,

$$[x, y, z]^{\text{new}} = [10\,x, y, z]^{\text{orig}} \tag{53}$$

This technique helps to highlight the additional half-planes of atoms close to the grain boundary.

To illustrate diffusional motion of atoms in the grain boundary, we color each atom with diffusive displacement δz larger than a few Burgers vectors. Figure 15 plots these atoms for several instants in time. Diffusion leads to significant surface grooving, with groove depths of up to several nanometers. One can clearly identify the wedge shape of the diffused atoms. The atomistic simulations show that atoms inserted into the grain boundary instantaneously crystallize, rendering the structure of the grain boundary invariant (this was observed for temperatures below 1150 K; at higher temperatures, the width of the grain boundary increases slightly). The atoms transported along the grain boundary may add to either one of the two grains, illustrating that the continuum mechanics assumptions [12, 18, 27] are also valid on the atomistic level. A frequently observed phenomenon is the emission of dislocations from the grain boundary on inclined $\langle 111 \rangle$ glide planes [6, 34], corresponding to the "classical" threading dislocations that become operative when stresses in the film are high enough to allow nucleation of dislocations [34, 36].
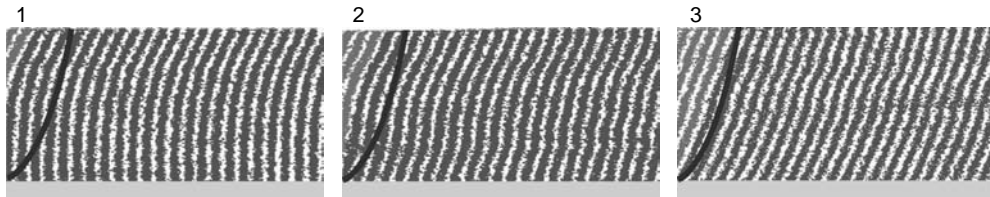

Figure 14. Lattice distortion near a diffusion wedge. The field becomes cracklike as the diffusion wedge builds up. The black lines correspond to the continuum solution of constrained grain boundary diffusion [12, 18] for $t \to \infty$.
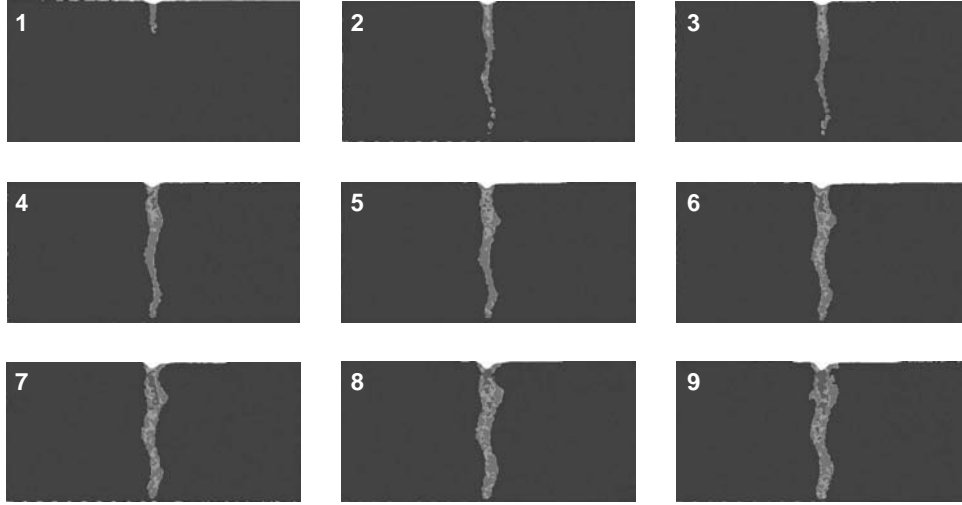
Figure 15. Formation of a grain boundary diffusion wedge. Atoms with significant diffusive displacement δz over time are highlighted. The plot shows that a diffusion wedge is formed by insertion of material into the grain boundary. The diffusion wedge develops at a relatively short timescale.

3.3. Atomistic Modeling of Nucleation of Parallel Glide Dislocations from Diffusion Wedges

Here we summarize the main results of the atomistic simulations that focused on the nucleation of parallel glide dislocations from diffusion wedges.

It was confirmed that thinner films require a higher critical stress for threading dislocation nucleation from the grain boundary, in qualitative agreement with the notion that the strength of thin films increases inversely to the film thickness [6]. In films thinner than 10 nm, extremely high stresses are required to nucleate inclined dislocations, which renders this mechanism almost impossible. This was also verified in a recent paper by Shen [42], in which the scaling of the strength of thin films with respect to the film thickness was investigated.

Continuum theory assumes that parallel glide dislocations are nucleated when the stress field around the diffusion wedge becomes cracklike. Critical stress intensity factors (SIFs) for dislocation nucleation measured from the atomistic simulations are shown in Table 2 for different simulations. Equation (37) was used to determine the SIF from the atomistic simulation results of the displacement field near the diffusion wedge. The critical SIF for the nucleation of parallel glide dislocations appears to be independent of film thickness and had similar values at $T_h = 0.8$ and $T_h = 0.9$.

For films thinner than 20 nm, parallel glide dislocations are not observed in our bicrystal model, as the cohesive strength of the film material is reached before the nucleation condition is met.

As reported in Refs. [28, 32], dislocation nucleation at a diffusion wedge can be divided into different stages, as shown in Fig. 16(a). After the critical SIF is achieved, a dislocation

Table 2. Critical stress intensity factors K^{PG} for nucleation of parallel glide dislocations near a diffusion wedge and a crack.

Temperature T (K)	Film thickness h_f (nm)	K^{PG} (MPa $\times$ m^s)
	Crack	
300	27.2	4.95
	Diffusion wedge	
1150	27.2	11.91
1250	27.2	11.35
1250	34.2	11.23

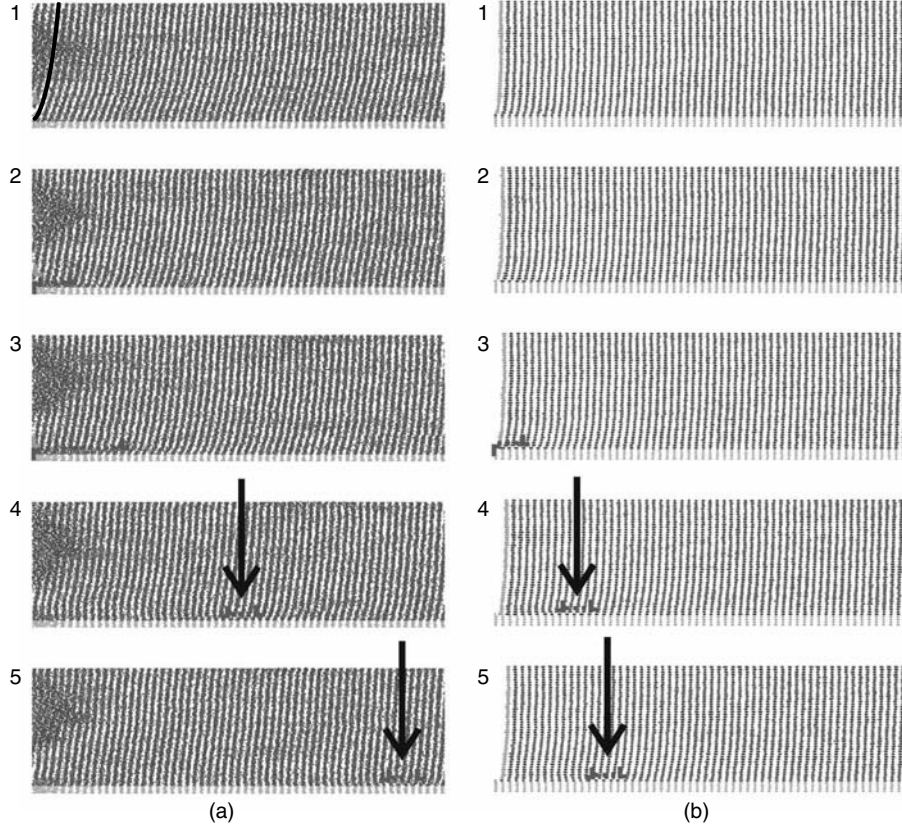*Source:* The data are taken from Ref. [28].

Figure 16. Atomistic details of the nucleation process of parallel glide dislocations from (a) a diffusion wedge and (b) a crack. The black line in the first snapshot of column (a) gives the solution of the continuum theory of constrained grain boundary diffusion [12, 18] for $t \rightarrow \infty$.

dipole is formed. One end of the dipole is pinned in the grain boundary, whereas the dislocation at the other end of the dipole slides away from the grain boundary. Subsequently, the pinned dislocation is annihilated or "dissolves into" the grain boundary, and the dislocation at the right end of the dipole begins to move away from the nucleation site. The parallel glide dislocation glides on a slip plane parallel to the plane of the film at a distance of a few Burgers vectors above the film–substrate interface (and is therefore completely inside the film material). The dislocation moves a small distance away from the grain boundary to its equilibrium position. When stresses in the film become larger, the film responds by moving farther away from the grain boundary. The nucleation process is highly repeatable. It was found that every time a parallel glide dislocation is nucleated, one climb edge dislocation is annihilated, leading to a decay in stress intensity. After a nucleation event, the time required to nucleate the next parallel glide dislocation is determined by the time required for diffusion to recover the critical stress intensity. This time increment is much less than the initial time required to form the diffusion wedge. After the first dislocation is nucleated, more and more parallel glide dislocations are observed. In our confined, finite simulation geometry, the emitted parallel glide dislocations form a "secondary pileup" close to the boundary of the simulation cell.

The nucleation of parallel glide dislocations from a crack in a similar geometry is shown in Fig. 16(b). The chosen loading rate was higher than in the previous case, and the temperature in the simulations was about 300 K. After an incipient dislocation is formed, a dislocation nucleates and moves away from the crack tip. The crack tip is blunted, and each time a parallel glide dislocation is nucleated, one surface step is formed. This process is also highly repeatable. The nucleation of parallel glide dislocations from a crack tip was observed at a loading rate a few orders of magnitude higher than in the case of a diffusion wedge, and there seemed to be no rate limitation in the case of a crack. As in the case of a diffusion

wedge, the dislocation glides on a parallel glide plane a few Burgers vectors above the film–substrate interface. The critical stress intensity factor for parallel glide dislocation nucleation from a diffusion wedge is about 2.3 times larger than that for a crack. This value was in good agreement with the estimated factor of two based on the Rice–Thomson model.

3.4. Discussion of Atomistic Simulation Results

When classical mechanisms of plastic deformation based on creation and motion of dislocations are severely hindered in thin films on substrates, constrained diffusional creep provides an important mechanism for stress relaxation, leading to the formation of a new type of defects called the grain boundary diffusion wedges. We have performed a set of large-scale atomistic simulations to investigate the properties of such diffusion wedges. Atomistic simulations show that material is indeed transported from the surface into grain boundaries and that such transport leads to a crack–like stress field causing the nucleation of parallel glide dislocations near the film–substrate interface. The atomistic simulations of parallel glide dislocations emitted near the root of the grain boundary have further clarified the mechanism of constrained grain boundary diffusion in thin films.

Computer simulations provide evidence that diffusion initiation occurs at a critical applied stress $\sigma_0^{\mathrm{crit}} \approx 1.6$ GPa in copper, independent of the film thickness. Continuum analysis in Eq. (34) at $T = 0$ K for initiation of diffusion supports this finding and predicts a critical stress $\sigma_0 \approx 6$ GPa, also independent of the film thickness. The fact that the continuum analysis indicates a higher value could be explained by the higher temperature used in the simulations, in contrast to the continuum mechanics analysis at 0 K. It was found in Ref. [43] that the critical stresses for dislocation nucleation are about five times smaller at room temperature than at 0 K, thus matching the value measured in the atomistic simulations. It has recently been shown that stress distribution in thin films over different grains is highly inhomogeneous [44]. In some grains, extremely high stresses of several GPa are observed. This provides sufficiently large stresses to initiate diffusion and a possible explanation of why parallel glide dislocation nucleation only occurs at specific grain boundaries in the experiments.

In films thinner than 10 nm, image stresses on climb dislocations can be as large as 1 GPa (see Section 2.3). This can severely hinder climb-mediated diffusional creep and indicates that the behavior of discrete dislocations needs to be considered in nanoscale thin films. This is supported by the atomistic results showing that stress cannot be completely relaxed in extremely thin films. These results are in qualitative agreement with experimental results that often show large residual stresses in extremely thin films [2].

The diffusion wedge has properties similar to a crack, but it requires a larger SIF to nucleate a dislocation. The reason for this is that in the case of a diffusion wedge, a dislocation dipole needs to be formed, and the dipole interaction force is twice as strong as the image force on an emergent dislocation near a crack tip. We have studied common and distinct properties observed in atomistic simulations of the two kinds of defects (crack versus diffusion wedge) along the grain boundary at elevated temperatures. For a crack, the following was observed: as the applied stress σ_0 is increased, the normal stress σ_{xx} along the grain boundary remains zero throughout the film thickness, consistent with the traction-free condition along the crack faces; the loading rate can be much higher than in the case of diffusional creep (there is no rate-limiting factor on dislocation nucleation); dislocation nucleation occurs at a relatively small stress intensity factor; and dislocation nucleation starts with an incipient dislocation close to the crack tip.

In contrast, for a diffusion wedge the following can be summarized: the loading rate must be slow enough for diffusion to remain as the dominant relaxation mechanism—at high loading rates, dislocation activities on inclined planes are observed instead of grain boundary diffusion; to nucleate a parallel glide dislocation, dislocation climb in the grain boundary must occur to annihilate part of an incipient dipole (on atomistic timescales, this is an extremely slow process—(for a crack, dislocation nucleation is fast); dislocation nucleation starts when the stress intensity factor reaches a critical value required to create a dislocation dipole near the diffusion wedge; and there exists a minimal thickness for parallel glide dislocation nucleation: If the film is very thin, the applied stress reaches the cohesive strength of the material before the critical stress intensity factor K^{PG} for dislocation nucleation is reached.

The two types of defects have significantly different timescales associated with dislocation nucleation. A crack is a ready source for dislocations, whereas a diffusion wedge has an intrinsic characteristic time associated with the dislocation climb. No essential difference in the mechanism of parallel glide dislocation nucleation from a diffusion wedge has been observed in the temperature range $0.8 < T_h < 0.9$.

4. EXPERIMENTAL STUDIES

Since its proposal in 1999, the model for constrained diffusional creep [12] has been further developed in light of experimental results [7, 35]. Weiss et al. [25] invoked the constrained diffusional creep model to explain the occurrence of a stress drop observed during the first heating cycle of thin copper films. They also used constrained diffusional creep to model the stress–temperature curves measured during thermal cycling of several films and found good agreement for a 500 nm copper film, albeit by assuming a very large grain size. Later, the discovery of parallel glide dislocations [45] provided experimental support for the constrained diffusional creep model. In turn, constrained diffusional creep furnished the basis for the interpretation of certain experimental results, especially in regard to the mechanisms for the creation and emission of parallel glide dislocations. In the following sections, we present key experimental results and their connection to the model of constrained diffusional creep.

4.1. Thermomechanical Behavior of Thin Copper Films

A series of thin copper films, ranging in thickness from 2 μm down to 35 nm, was produced by magnetron sputtering under ultrahigh vacuum. All films were annealed immediately thereafter in the deposition chamber, without breaking vacuum, yielding oxide-free unpassivated copper films. The substrates used for the films were (001)-oriented single crystalline silicon that had been coated with 50 nm amorphous silicon oxide and 50 nm amorphous silicon nitride before copper deposition. Thus, the interface between film and substrate is crystalline/amorphous. The average grain size, as determined from focused ion beam (FIB) and transmission electron microscopy (TEM) measurements, ranged from 1.5 times the film thickness (for the 2-μm film) to 2.5 times the film thickness (for the 100-nm film). X-ray diffraction measurements revealed that all films had a strong [111] fiber texture, albeit with a small population of [100]-oriented grains for films thicker than 200 nm. Thus, the vast majority of grains within each film, including the grains imaged using TEM and presented below, are oriented with a (111) plane parallel to the substrate.

The thermomechanical behavior of each film was determined by subjecting it to a thermal cycle between room temperature and 500°C. Because copper possesses a higher coefficient of thermal expansion than silicon, an equibiaxial compressive stress evolves in the film during heating, and a tensile stress evolves during cooling. This coupling of stress and temperature in the film/substrate system enables the thermomechanical loading of thin films, and a variety of thermal paths can be employed to generate compressive and tensile stresses of varying magnitude. In the examples presented below, simple thermal cycles starting at room temperature, progressing up to 500°C and then returning to 50°C were performed. Heating and cooling rates were 6 K/min, except for final cooling below 100°C, which proceeded at 4 K/min because of the limited cooling capacity of the oven.

An example of the thermomechanical behavior of an ultrathin copper film is presented in Fig. 17. The stress within this 100-nm film was initially 360 MPa. During heating, the tensile stress decreased and a compressive stress was achieved by 210°C. The compressive stress rose in magnitude with further heating but then dropped after reaching a maximum at 260°C. The stress level decreased slightly during heating to 320°C and then became more compressive during heating to 500°C. From this point on, the stress evolution was monotonic with temperature: cooling produced a tensile stress and subsequent heating in the second cycle produced a compressive stress again. No stress drops were observed in the second cycle or later.

The stress drop that occurs above 250°C in the 100-nm film, as well as in all thicker films measured in this study, appears to be the result of constrained diffusional creep, as previously
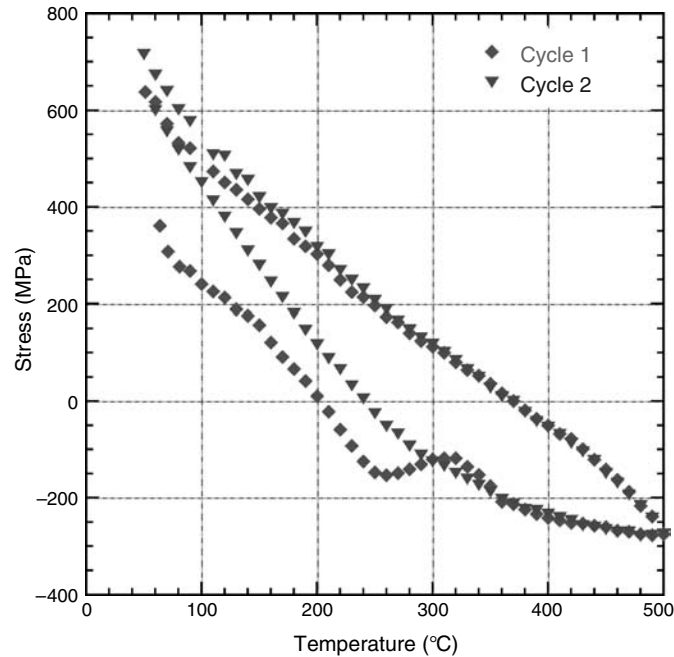
Figure 17. The first two thermal cycles of a 100-nm copper film. During the first heating segment, a stress drop is observed at 260°C, which is attributed to constrained diffusional creep. Subsequent thermal cycles are highly repeatable, with no stress drop.

explained by Weiss et al. [25]. The temperature of 250°C, which represents a homologous temperature of 0.4, is apparently sufficient to activate surface and grain boundary diffusion and lead to the formation of diffusion wedges during heating. Only when the relaxation of stress at the grain boundaries is saturated, in this case at a temperature well above 300°C, does stress increase again. The lack of the stress drop during the second and later thermal cycles is explained by the stress level: at 250°C in the second cycle, film stress is only −26 MPa, which may be insufficient to cause outward diffusion of copper atoms from the grain boundaries, and therefore no stress relaxation occurs.

The second cycle in Fig. 17 deviates from the first cycle during the final stages of cooling (below ∼200°C), perhaps because of the thermal drift of the sample. This, however, is an inherent error in the experimental technique and gives a good measure of the error one should assign to the absolute stress values that are reported. The film strength is typically taken to be the flow stress measured at the end of a thermal cycle. Thus, in this case, the strength of the 100-nm film would simply be given by the average of the two stresses measured at 50°C at the end of cooling: 676 ± 39 MPa.

Although film strength generally increases with decreasing film thickness [2, 25, 46], unpassivated copper films deviate from this trend below 400 nm [7]. Instead of rising continuously, the film strength exhibits a plateau between 650 and 700 MPa for films 400 nm and thinner. This is apparent in Fig. 18, which shows the second thermal cycle for a 200-nm copper film, along with the second cycle for the 100-nm film from Fig. 17. The two films exhibit virtually identical thermomechanical behavior, with the film strengths at 50°C (695 ± 9 MPa for the 200-nm film) and the flow stresses at 500°C matching very closely. Although the 500°C flow stress does become slightly more compressive in thinner films, the plateau in 50°C film strength persists down to a thickness of 35 nm.

To explore whether the stress–temperature cycles, such as those shown in Figs. 17 and 18, represent steady-state behavior, a 50-nm copper film was thermally cycled at two different rates. In addition to the standard 6 K/min rate, a complete cycle was performed at 1 K/min; both are portrayed in Fig. 19. Because of the extremely small film thickness, this comparison allows us to investigate whether grain boundary diffusion and constrained diffusional creep are able to proceed to completion within the time frame of these experiments. The heating segments of each cycle are somewhat different, but they yield roughly the same 500°C
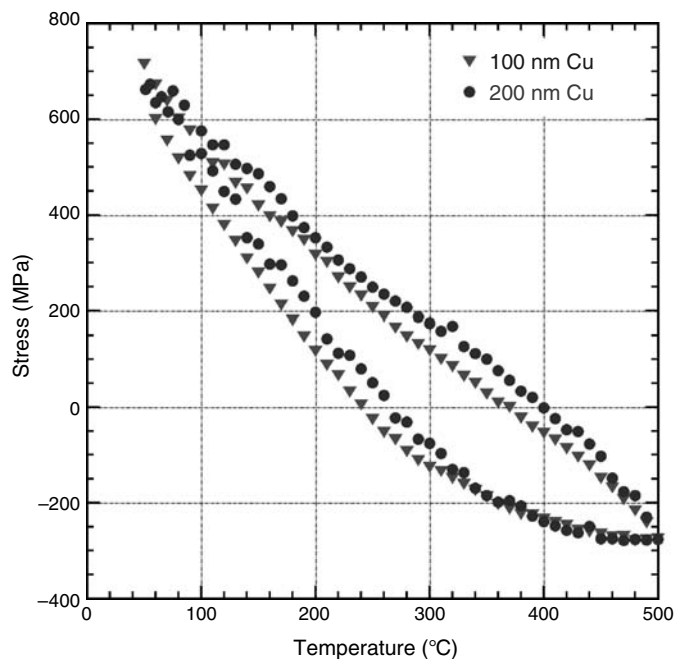
Figure 18. The second thermal cycle of a 200-nm copper film, along with the second cycle of the 100-nm film from Fig. 18. Both films exhibit the same thermomechanical behavior, with the same stress levels at 500° and 50°C.

flow stress; namely, 322 ± 14 MPa. However, there is a large discrepancy in stress evolution during cooling, especially between 350° and 200°C. Within this temperature range, the lower cooling rate permits significantly more stress relaxation. This indicates that the standard 6 K/min used throughout this study is too fast to allow constrained diffusional creep to reach steady state and that grain boundary diffusion may be the rate-limiting step in this
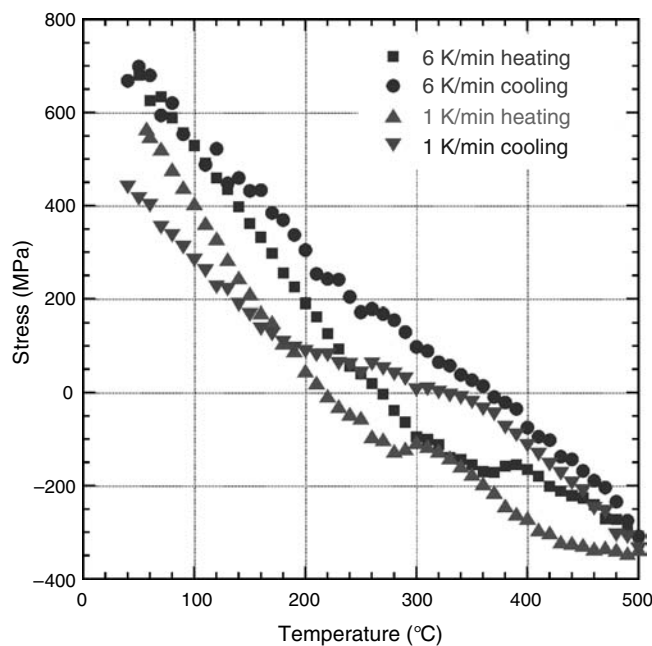

Figure 19. Two thermal cycles of a 50 nm copper film, conducted at different heating and cooling rates. Although the same 500°C flow stress is reached in both cases, the stress evolution during cooling is seen to depend strongly on cooling rate, indicating that the standard rate of 6 K/min is too fast to allow constrained diffusional creep to proceed to completion.

temperature regime. The final cooling curves below 200°C appear to be offset by approximately 200 MPa, but they exhibit the same slope, indicating that constrained diffusional creep is equally slow in both cases, or that constrained diffusional creep is no longer able to provide stress relaxation below 200°C.

4.2. Transmission Electron Microscopy Observations of Dislocation Behavior

Thermal cycling experiments were also conducted *in-situ* in the TEM to elucidate the deformation mechanisms underlying the thermomechanical behavior illustrated in Figs. 17–19. These figures clearly showed that films in this thickness range ($\leq$200 nm) exhibit a plateau in strength, which indicates that the Mathews–Freund–Nix mechanism involving threading dislocations is saturated or has been replaced. As discussed below, *in-situ* observations of dislocation motion revealed that a new, alternative deformation mechanism does indeed dominate in ultrathin, unpassivated copper films.

Figure 20 shows an example of parallel glide dislocations in a small grain within a 200-nm copper film. There are four dislocations oriented roughly perpendicular to the diffraction vector **g** in the TEM micrograph. During subsequent heating, these dislocations moved in the direction of **g** and underwent glide across the entire width of the grain. In this image of the [111]-oriented grain, the projected width of all inclined {111} planes is 70 nm. On the basis of their length and the extent of their motion (up to 300 nm), the dislocations must therefore have moved on the (111) plane parallel to the film/substrate interface. Because of this, the observed motion was termed "parallel glide" [7].

An important consequence of glide occurring parallel to the film/substrate interface is that the Burgers vector of the dislocations, which must lie within the (111) glide plane, is parallel to the plane of the film. However, the biaxial film stress that evolves in the film during thermal cycling does not produce a resolved shear stress on this plane, and it therefore cannot be directly responsible for the motion of parallel glide dislocations. Both of these points, however, are addressed by the constrained diffusional creep model [12], which aids the interpretation of these experimental results. As predicted by the theoretical simulations and discussed further below, parallel glide is a consequence of constrained diffusional creep.

Additional experimental observations have clarified several details of this deformation mechanism. Figure 21 shows another example of parallel glide dislocations, extending from
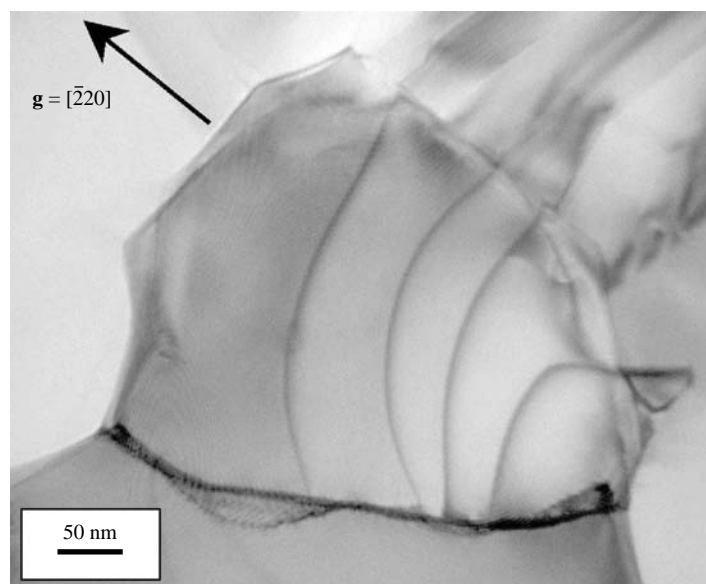

Figure 20. Transmission electron micrograph of parallel glide dislocations in a 200-nm copper film. These edge-oriented dislocations underwent glide in the direction of the diffraction vector **g**. On the basis of the extent of their motion, the only possible glide plane is the (111) plane parallel to the film–substrate interface.
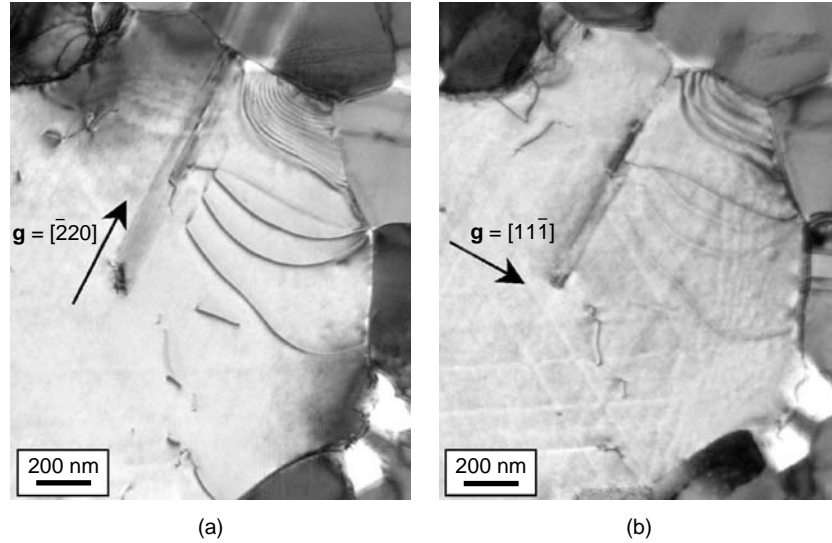
Figure 21. (a) Three parallel glide dislocations are visible in this transmission electron (TEM) micrograph of a 200-nm copper film. Their (111) glide plane, which is also the plane of this image, contains the Burgers vector **b**. (b) TEM of the same location, but with a different diffraction vector. The three parallel glide dislocations are invisible here, indicating that **b** is perpendicular to [11$\bar{1}$]. On the basis of these images, **b** must be parallel to [$\bar{2}$20], and the dislocations thus have predominantly edge character.

the twin in the middle of the micrographs to the grain boundary at the right. In Fig. 21(a), three dislocations are visible, but in Fig. 21(b), they are invisible, indicating that the Burgers vector is perpendicular to the [11$\bar{1}$] direction. Moreover, the Burgers vector lies within the (111) plane and must therefore be parallel to the [$\bar{2}$20] diffraction vector in Fig. 21(a). The dislocations thus have predominantly edge character, as they are oriented roughly perpendicular to **b** and **g** in Fig. 21(a). This is a general feature of parallel glide dislocations, which are always emitted with edge character. During subsequent glide, which can involve interaction with other dislocations and with obstacles such as twins and grain boundaries, the parallel glide dislocations may bow into a curved shape and attain mixed character.

In-situ TEM observations [7] have revealed that parallel glide dislocations are emitted from sources at triple junctions and grain boundaries. Typically, these grain boundaries (or one of the grain boundaries leading to the triple junction) are oriented roughly perpendicular to the Burgers vector. This indicates that the diffusion wedge added to the grain boundary is indeed essentially an array of edge dislocations, which are eventually emitted and that undergo parallel glide.

In all cases in which it was measured [7, 45], the tilt angle between grains bounding a parallel glide source was found to lie between 6° and 6.5°. Tilting and diffraction experiments near a ⟨112⟩ zone axis revealed that the tilt angle is 6°, not 66° (i.e., the 60° ambiguity inherent to the comparison of [111] electron diffraction patterns was eliminated). This provided a key piece of information for input into the atomistic simulations [28, 30, 32] and allowed the introduction of grain boundaries that were suitable for constrained diffusional creep and the emission of parallel glide dislocations in the simulated cooling experiments.

By tilting the specimen, one can image the inclined grain boundaries and observe the position of parallel glide dislocations by determining exactly where they terminate. TEM micrographs [7] reveal that the dislocations meet the grain boundaries at the film–substrate interface. Thus, the parallel glide plane is located at the bottom of the grain, albeit some small distance above the silicon nitride. From high-resolution TEM micrographs [47], it was observed that the silicon nitride layer is not atomically flat but, instead, contains hills and valleys, with a peak-to-valley height of approximately 2 nm. Given the observation that parallel glide occurs over large distances, without cross-slip events, the glide plane cannot lie directly at the film–substrate interface, but instead must be situated several nanometers above it.

Multiple families of parallel glide dislocations are sometimes also observed, as shown in Fig. 22. Three families, each oriented roughly perpendicular to one of the three $\langle \bar{1}10 \rangle$ directions within the (111) film plane, are located at the bottom, right, and top-left corners of the grain. In contrast to other examples of parallel glide (e.g., Fig. 19), the dislocations in Fig. 22 accommodate strain symmetrically within the film plane. This appears to be a result of the grain size, as smaller grains rarely exhibit multiple families of dislocations.

Finally, copper films passivated with an aluminum oxide layer were also investigated for comparison with the observations of the unpassivated films presented above. Although their thickness and grain size are identical to the unpassivated films, passivated films do not exhibit parallel glide. Instead, threading dislocations are generated. As they glide through the film on inclined {111} planes, they deposit straight segments along $\langle 110 \rangle$ directions at the film–substrate interface, as shown in Fig. 23. Passivation of the film surface completely shuts down parallel glide, providing strong evidence that surface diffusion is an essential component of this deformation mechanism.

4.3. Interpretation of Experimental Observations

The observations of parallel glide can be explained with the help of the constrained diffusional creep model. The finding that an unpassivated film surface is required for parallel glide supports the claim that constrained diffusional creep is the mechanism responsible for stress relaxation and plastic deformation in ultrathin copper films. The stress drop observed during the first heating cycle of a copper film (e.g., in Fig. 17) is explained nicely by the constrained diffusional creep model. Finally, other models of thin film deformation are unable to explain parallel glide, as the biaxial film stress that evolves during thermal cycling does not generate a resolved shear stress on the (111) plane parallel to the substrate and therefore cannot directly drive the dislocation motion presented here.

Because parallel glide is the dominant mode of dislocation motion in copper films 200 nm thick and thinner, and as parallel glide appears to be a consequence of constrained diffusional creep, we can check whether constrained diffusional creep mediates the entire amount of plasticity during a thermal cycle. According to the constrained diffusional creep model, atoms diffuse from the surface into the grain boundaries of a film under tension, assuming that temperature and stress are sufficiently high. For an appropriately oriented grain, this
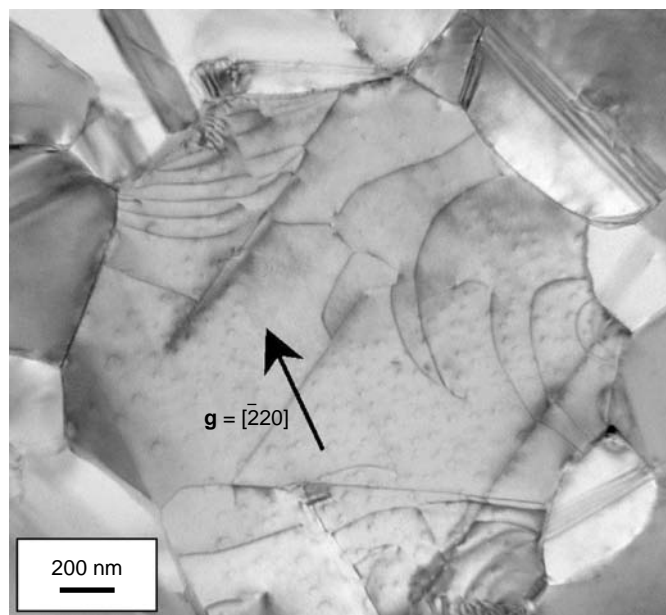

Figure 22. Transmission electron micrograph of a grain exhibiting multiple families of parallel glide dislocations, one each at the bottom, right, and top left corners of the grain. The families are each oriented roughly perpendicular to one of the three $\langle \bar{1}10 \rangle$ directions within the (111) film plane.
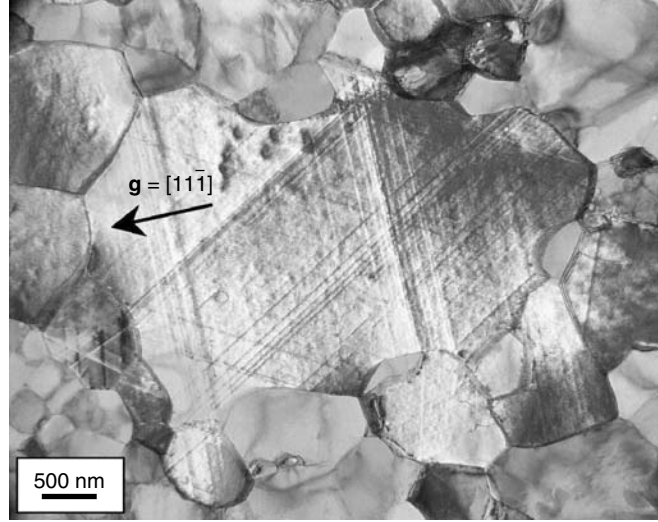
Figure 23. When passivated with an aluminum oxide layer, 200-nm copper films no longer exhibit parallel glide. Instead, threading dislocations are activated, which glide through the film and generate straight slip traces at the film–substrate interface.

is equivalent to adding edge dislocations at the grain boundary. For each edge dislocation, the addition of the extra half-planes increases the grain length by b, the magnitude of the Burgers vector. We can therefore calculate how many parallel glide dislocations should exist within a given grain:

$$d_{\text{grain}} \varepsilon_{\text{plastic}} = N_d b \tag{54}$$

where d_{grain} is the grain length parallel to **b**, $\varepsilon_{\text{plastic}}$ is the plastic strain measured from the stress–temperature plot for a thermal cycle, and N_d is the number of parallel glide dislocations.

Application of Eq. (54) to TEM observations yields excellent agreement. In Fig. 24, a schematic of the grain and parallel glide dislocations from Fig. 20, tilted back to simulate a three-dimensional view, has been drawn. The parallel glide plane, shaded gray in the figure, is located at the bottom of the grain, near the film–substrate interface. The dislocations are roughly perpendicular to **b** and are distributed over the length of the grain. The relevant values for Eq. (54) are $d_{\text{grain}} = 400$ nm and $\varepsilon_{\text{plastic}} = 0.30\%$ for a 200-nm copper film. The required number of dislocations is thus $N_d = 4.7$. Four dislocations were observed in the grain. The remainder, 0.7, is insufficient to necessitate the emission of a fifth dislocation.
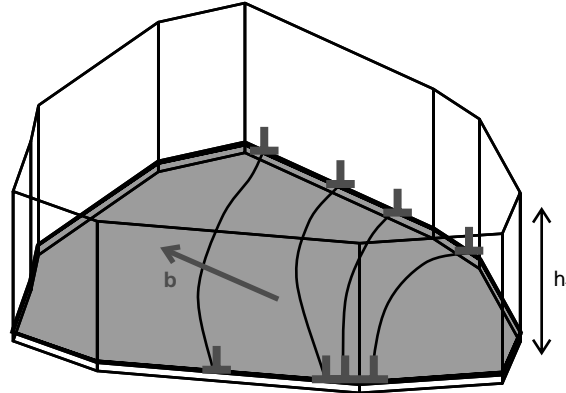

Figure 24. Schematic of the grain and parallel glide dislocations from Fig. 20. The glide plane is at the bottom of the grain, near the film–substrate interface, and the dislocations are distributed across the width of the grain. The number of parallel glide dislocations corresponds to the average amount of plastic strain exhibited by the film during thermal cycling.

More specifically, however, this "missing" partial dislocation should simply remain in the grain boundary, as there is no driving force for its emission.

In other words, a criterion for the occurrence of parallel glide is the presence of multiple dislocations in a grain boundary. Once an additional dislocation, or perhaps a partial dislocation, is formed in the grain boundary, the repulsive force between them causes the emission of the first dislocation into the grain. Based on comparisons between Eq. (54) and TEM observations, the presence of a partial dislocation appears to be the more likely case. This leads to a slightly modified equation that accounts for the emission criterion:

$$d_{\mathrm{grain}}\varepsilon_{\mathrm{plastic}} = \left(N_d + \frac{1}{2}\right)b \qquad (55)$$

For larger grains, where many dislocations should undergo glide, the difference between Eqs. (54) and (55) may be insignificant. However, as grain size decreases toward the nanoregime, the exact form of Eq. (55) becomes important. The additional 1/2 may need to be replaced by a different quantity, but this possibility requires further investigation.

A consequence of Eqs. (54) and (55) is that there is a critical length scale for the formation of a parallel glide dislocation; namely, roughly $b/\varepsilon_{\mathrm{plastic}}$. In grains smaller than this quantity, less than a single dislocation is required to mediate the entire amount of plasticity. In this case, the partial dislocation remains in the grain boundary. Indeed, almost no dislocation motion is observed in 50-nm copper films, which undergo a plastic strain of 0.25% during a thermal cycle and therefore have $b/\varepsilon_{\mathrm{plastic}} = 102$ nm. The median grain size in a 50-nm copper film is only 99 nm (i.e., more than half of the grains require less than a single parallel glide dislocation, and only a small minority of the grains are sufficiently large [>150 nm] for parallel glide to occur at all). In 50-nm films, parallel glide was observed in relatively large grains (i.e., >200 nm), supporting the concept of a critical length scale.

The multiple families of parallel glide dislocations in Fig. 22 indicate that plastic strain is accommodated along all possible $\langle\bar{1}10\rangle$ directions within the (111) film plane, as should be the case for an equibiaxial stress state. In many cases, especially in smaller grains, parallel glide occurs in only one or two directions. This is likely a result of the character of the remaining grain boundaries, which may allow some degree of diffusion but still be unsuitable for the emission of parallel glide dislocations. In addition, in small grains, the emission of parallel glide dislocations from a grain boundary may alter the stress state sufficiently to hinder the insertion of diffusion wedges into the remaining grain boundaries.

Copper films with 200 nm thickness have been presented here to illustrate parallel glide. Although these films, which yielded the TEM observations presented above, are thicker than those that were simulated, it has been experimentally confirmed [7] that parallel glide is the dominant mode of dislocation motion in films between 50 and 200 nm thick. Note that 50-nm films exhibit little dislocation activity, but that which does occur always takes place via parallel glide.

Parallel glide is a consequence of constrained diffusional creep (i.e., the actual deformation mechanism is constrained diffusional creep). The motion of parallel glide dislocations does not mediate plasticity. Rather, it redistributes, across the width of the grain, the strain fields of the edge dislocations contained within the diffusion wedges. By the time parallel glide occurs, constrained diffusional creep has already provided plastic strain by increasing the grain dimension. Thus, in terms of strain accommodation, it does not matter where the parallel glide dislocations are situated within the grain. This is fundamentally different from conventional dislocation slip and threading dislocation motion, which progressively mediate plastic strain as glide occurs.

5. MODELING THE EXPERIMENTAL RESULTS WITH CONTINUUM THEORY

In addition to aiding the interpretation of the TEM observations of parallel glide, the constrained diffusional creep model can be used to generate the stress–temperature curve for a thermal cycle. This was done by Weiss et al. [25] for copper films, although certain discrepancies between simulated and experimental curves could not be overcome. The model has

since been modified to include a threshold stress for constrained diffusional creep, which has led to better agreement in the high-temperature regime, as presented below.

5.1. Experimental Estimate of the Threshold Stress

Experimental results provided an estimate of the threshold stress in thin copper films. Constant-temperature stress relaxation experiments were performed with films ranging in thickness from 100 nm to 2 μm. During cooling from 500°C, the sample was held at 250°C for 16 h, and the amount of stress reduction was monitored. The final stress measured in each film is listed in Table 3. For film thicknesses between 100 nm and 1 μm, the relaxed stress level is very consistent, with an average value of 81 MPa [see also Fig. 10(b)]. This is surprising, given the large variation in stress as a function of film thickness, as determined from standard thermal cycles. Only the 2-μm film exhibits a lower stress.

The data in Table 3 indicate that the concept of a threshold stress for constrained diffusional creep is valid for all copper films below micrometer size. It is also in agreement with the notion of an athermal stress component in thin films, as discussed by Kobrinsky et al. [2, 48, 49]. The athermal stress cannot be relaxed by thermally activated mechanisms such as constrained diffusional creep. Kobrinsky's results [2, 48] also indicate a thickness-independent threshold stress for silver films between 250 and 860 nm.

5.2. Fit of the Continuum Theory to Experimental Results

In this section we discuss some fits of the extended continuum mechanics model with threshold stress to the experimental results.

5.2.1. Modeling of Thermal Cycling Experiments

As reported in Refs. [25, 50], the grain boundary diffusivity for copper is given by

$$\delta_{\mathrm{gb}} D_{\mathrm{gb}}(T) = 5 \times 10^{-15} \exp\left(-\frac{Q_b}{\mathrm{R}T}\right) \mathrm{m^3\,s^{-1}} \qquad (56)$$

with activation energy $Q_b = 104$ kJ/mole. We consider two film thicknesses of 100 and 600 nm. The threshold stresses for the grain boundary average stress is estimated from the experimentally measured average stress in the film by Eq. (32) and are approximated to be $\sigma_t^+ = 65$ MPa and $\sigma_t^- = -65$ MPa. In the following text we assume that $E = 124$ GPa, $\nu = 0.34$ and $\Delta\alpha = 1.3 \times 10^{-5}$ K^{-1}. In Figs. 25 and 26 we show a comparison between experiment and the continuum model with threshold stress for steady-state thermal cycling of thin films of thickness $h_{\mathrm{f}} \approx 100$ nm (Fig. 25) and 600 nm (Fig. 26).

In both cases, some qualitative agreement is found, especially at elevated temperatures. For the 600-nm film, the agreement at low temperatures during the cooling cycle (upper curve) is not as good as for high temperatures. This could partly be explained by the fact that, because of the rather large film thickness, not only parallel glide dislocations present, but threading dislocations are also nucleated and relieve stresses, as observed in the experiment in Ref. [7]. During cooling of the film, diffusional creep dominates at high temperatures, but threading dislocations may dominate at low temperatures. Because the continuum model does not account for threading dislocations, the stresses at low temperatures (upper left corner in the plot) are overestimated. At high temperatures during the heating cycle, the stress at the grain boundary relaxes to the value associated with the threshold stress σ_t^-, and

Table 3. Average film stresses measured after isothermal relaxation at 250°C for 16 h.

h_{f} (nm)	100	200	800	1000	2000
$\sigma_{250°C,\,\text{relaxed}}$	80	73	85	85	43

Note: All films between 100 nm and 1 μm exhibit nearly the same stress, with an average value of 81 MPa. On the basis of the experimental data, 65 MPa was taken to be the threshold stress at the grain boundary; that is, the high-temperature flow stress of thin copper films following maximum relaxation by constrained diffusional creep.
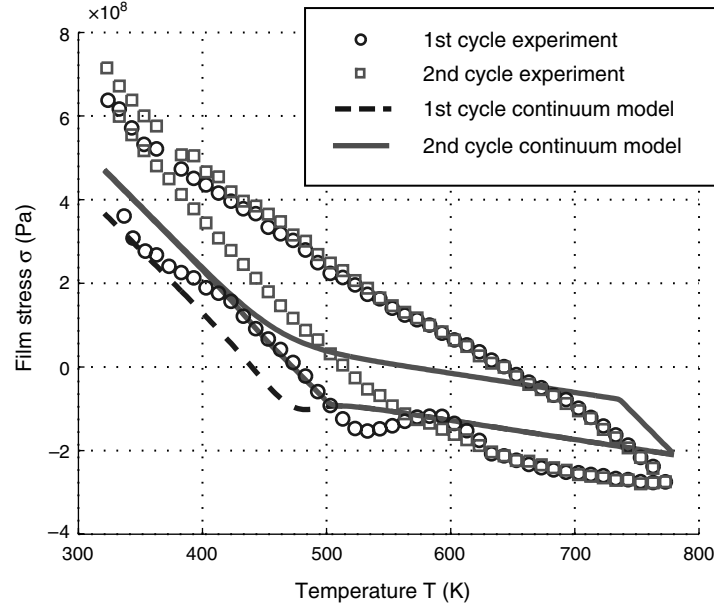
Figure 25. Fit of continuum model with threshold stress to the experimental data from Fig. 17. The film thickness is $h_f = 100$ nm and grain boundary diffusivities are as in Ref. [50].

the experimental measurements and continuum modeling of the average stress in the film agree quite reasonably.

The fits show that the introduction of a threshold stress based on experimental data represents an improvement of the previous model. Unlike in Ref. [25], where the grain size had to be adjusted to improve agreement, the parameters used here are identical to those used in the experiments (same grain size, same ratio of grain size to grain diameter, same cooling and heating rates, etc.). The most important difference is that without the threshold stress, the numerically estimated curves are very "thin" in contrast to the experimental results. The thermal slope, which is apparent at high temperatures during the cooling cycle, can only be reproduced with the generalized model, including a threshold stress.
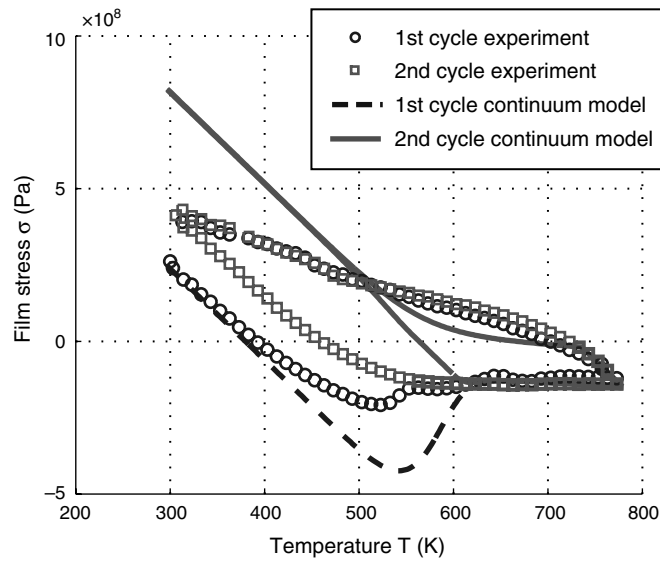

Figure 26. Fit of continuum model with threshold stress to experimental data. The film thickness is $h_f = 600$ nm and grain boundary diffusivities are as in Ref. [50].

5.2.2. Estimation of Diffusivities from Experimental Data

Another interesting aspect is the estimation of diffusivities from the experimental data. It can be observed in Fig. 26 that the stress decrease in the first heating cycle is larger in the experiment than in the simulation. When the diffusivities reported in the literature are used, the maximum compressive stress is overestimated by a factor of two (a similar observation was also made in the paper by Weiss et al. [25], Fig. 10). This could be because the diffusivities used in the continuum mechanics model are smaller than the actual experimental value. Figure 27 shows a fit of the continuum mechanics model to the experimental data, with a threshold stress $\sigma_t^- = -65$ MPa for a 600-nm film, as obtained from experiment (see discussion above). Fitting the maximum compressive stress to the experimental results by adjusting the diffusivity yields a diffusivity 80 times higher than in the literature. Possible reasons for this could be the fact that the grain boundary structure strongly influences the diffusivities. In the literature, a dependence of the diffusivities on grain boundary structure has been proposed (for further discussion, see, for instance, Refs. [28, 35]). Such considerations, have not been taken into account in modeling diffusion in thin films so far, but they may explain the observations discussed above.

The fitted grain boundary diffusivity is given by

$$\delta_{gb}D_{gb}(T) = 4 \times 10^{-13} \exp\left(-\frac{Q_b}{RT}\right) m^3 s^{-1} \tag{57}$$

The characteristic time for a film with $h_f = 20$ nm at a temperature of about 90% of the melting point is then on the order of 10^{-8} s. This supports the idea that constrained grain boundary diffusion can be modeled with classical molecular dynamics, as such simulations are typically limited to a timescale of around 1×10^{-8} s [28, 33].

Finally, we compare calculations with the new estimate for diffusivities to the experimental results. In Fig. 28 we show a comparison of experiment and the continuum model with threshold stress for steady-state thermal cycling of thin films with film thickness $h_f \approx 100$ nm. In Fig. 29 we show a comparison of experiment and the continuum model with threshold stress for film thickness $h_f \approx 600$ nm.

6. MAP OF PLASTIC DEFORMATION MECHANISMS

The results from the numerical modeling together with the experimental findings [7] were used to qualitatively describe different deformation mechanisms that occur in sub-micron thin films. It was proposed in Ref. [30] that there exist four different deformation regimes: (1) deformation with threading dislocations, (2) constrained diffusional creep with
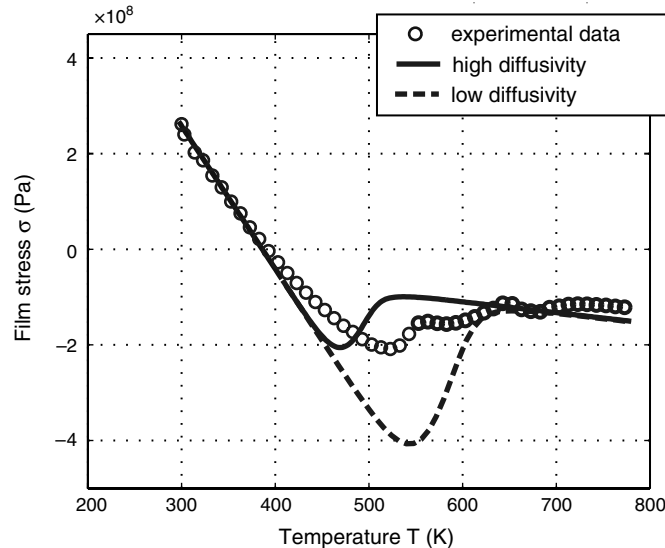

Figure 27. Fit of diffusivities to the experimental data based on the first heating curve of the 600-nm film.
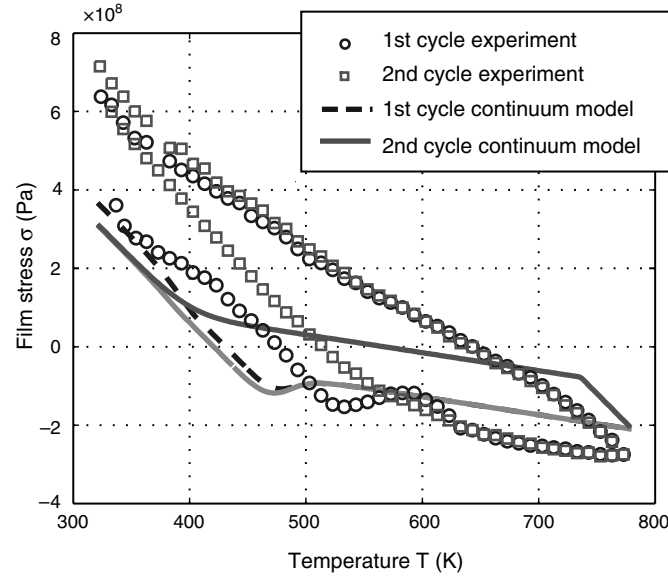
Figure 28. Fit of continuum model with threshold stress to experimental data. The film thickness is $h_f = 100$ nm, and grain boundary diffusivities are fitted to experimental data.

subsequent parallel glide, (3) constrained diffusional creep without parallel glide, and finally, for the thinnest films, and (4) no stress relaxation mechanism (no diffusion and no dislocation motion possible). A schematic "deformation map" is plotted in Fig. 30. This plot shows the critical applied stress to initiate different mechanisms of deformation as a function of the film thickness. Note that it is assumed that loading is applied very slowly and that temperature is sufficiently high for diffusive processes to occur.

The critical applied stress to nucleate threading dislocations scales with $1/h_f$ [4–6]. The $1/h_f$ scaling has also been found in two-dimensional molecular dynamics simulations [34]. For films thicker than a material-dependent value, regime (1) is the dominant deformation mechanism. For thinner films, the stress necessary to nucleate threading dislocations is larger than that required to initiate grain boundary diffusion. In this regime (2), diffusion dominates stress relaxation and causes a plateau in the flow stress, as shown by experimental results
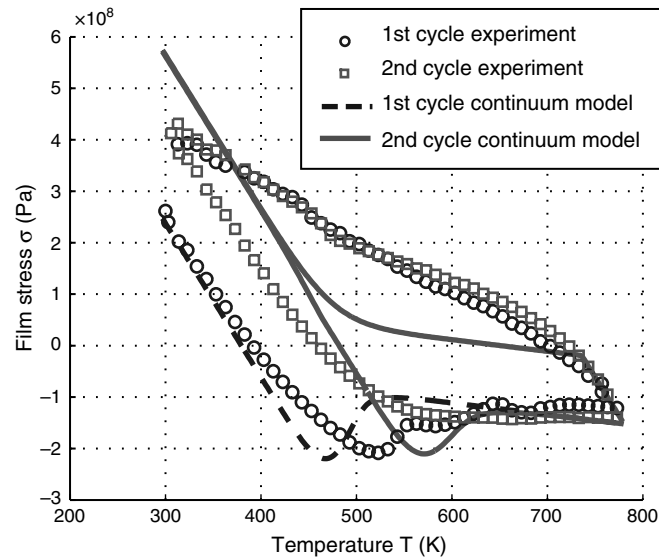

Figure 29. Fit of continuum model with threshold stress to experimental data. The film thickness is $h_f = 600$ nm, and grain boundary diffusivities are fitted to experimental data.
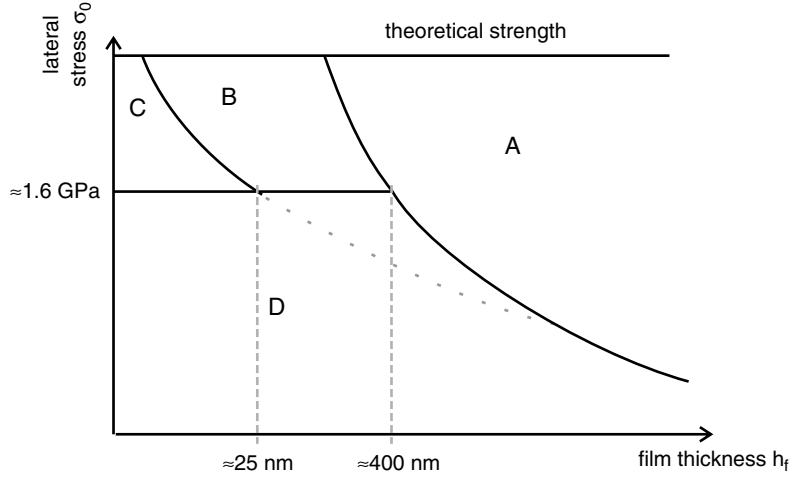
Figure 30. Deformation map of thin films as a function of film thickness, summarizing different stress relaxation mechanisms in ultrathin films on substrates [30].

[7, 8] and later by discrete dislocation modeling [31]. Parallel glide helps to sustain grain boundary diffusion until the overall stress level is below the diffusion threshold, which is independent of the film thickness. For yet thinner films, our MD simulations revealed that grain boundary diffusion stops before a sufficient stress concentration for triggering parallel glide is obtained. The onset of regime (3) can be described by the scaling of the critical nucleation stress for parallel glide with $1/h_{\mathrm{f}}^{s}$ ($s = 0.5$ for the homogeneous film/substrate case). In this regime, the flow stress again increases for smaller films because of due to the back stress of the climb dislocations in the grain boundary, effectively stopping further grain boundary diffusion. If the applied stress is lower than the critical stress for diffusion, no stress relaxation is possible. This is referred to as regime (4).

The yield stress of thin films resulting from these considerations is summarized in Fig. 31 for different film thicknesses. For thicker films, the strength increase is inversely proportional to the film thickness, as has been shown in several theoretical and experimental studies [1, 5, 7, 9]. If the film thickness is small enough such that grain boundary diffusion and parallel glide are the prevailing deformation mechanisms, the film strength is essentially independent of h_{f}, as seen in experiment [7] and as later shown by the discrete dislocation model [31]. However, for films thinner than $h_{\mathrm{f}} \approx 30$ nm, discrete dislocation modeling [31] predicts again an increase in strength with decreasing film thickness.
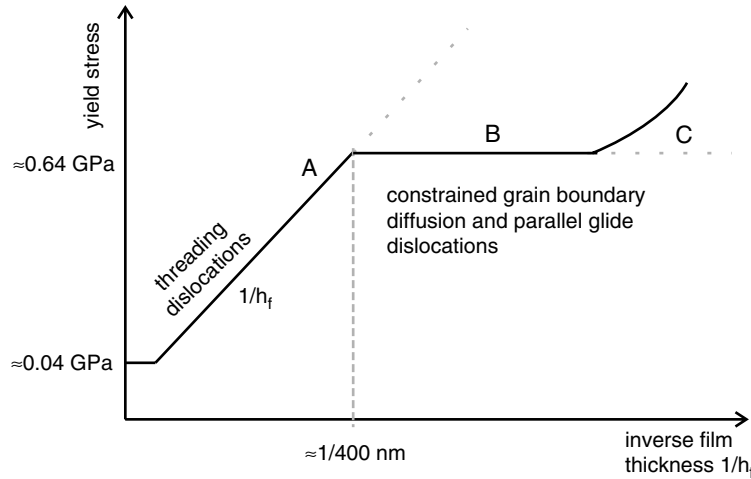

Figure 31. Strength of thin films as a function of film thickness. The film thickness of $h_{\mathrm{f}} \approx 400$ nm, as well as the plateau yield stress of 0.64 GPa, are taken from experimental results [7, 8]. Further details are given in Ref. [30].

The existing understanding is mostly qualitative. A few data points from experiment, simulation, or theory were taken to draw the deformation map. Future studies could focus on a more quantitative study of the different deformation mechanisms and provide a systematic study of transition from one regime to the other. Mesoscopic simulations [31], as applied to constrained diffusional creep and nucleation of parallel glide dislocations, could play an important role in these studies.

7. SUMMARY AND CONCLUSIONS

In this chapter we have reviewed recent theoretical, numerical, and experimental activities investigating the mechanical properties of submicron thin films on substrates.

Theoretical modeling predicted the existence of so-called grain boundary diffusion wedges. This model was later successfully used to explain experimental observations of parallel glide dislocations, which verified the prediction that dislocations with Burgers vector parallel to the film plane could be emitted from the tip of a diffusion wedge. The experimental results, together with the theoretical predictions, guided molecular dynamics studies that confirmed this concept at the atomic scale.

A new and significant result reported in this chapter is the modeling of thermal cycling of ultrathin films using continuum theories. With the new concept of a threshold stress, we qualitatively reproduced experimental results. Additional discussion was devoted to estimates of the grain boundary diffusivity from experimental data. It was found that diffusivities are higher than reported in the classical literature [50], which may be attributed to the dependence of diffusivities on the grain boundary structure. A deformation map describing numerous novel deformation mechanisms in thin metal films was developed to summarize the main findings.

The examples reported in this chapter exemplify the richness of phenomena that can occur as the dimensions of materials shrink to nanometer scale.

ACKNOWLEDGMENTS

REFERENCES

 1. R.-M. Keller, S. P. Baker, and E. Arzt, *Acta Mater.* 47, 415 (1999).
 2. M. J. Kobrinsky and C. V. Thompson, *Appl. Phys. Lett.* 73, 2429 (1998).
 3. R. P. Vinci, E. M. Zielinski, and J. C. Bravman, *Thin Solid Films* 262, 142 (1995).
 4. L. B. Freund, *J. Appl. Mech.* 54, 553 (1987).
 5. W. D. Nix, *Metall. Trans. A* 20, 2217 (1989).
 6. W. D. Nix, *Scripta Mater.* 39, 545 (1998).
 7. T. J. Balk, G. Dehm, and E. Arzt, *Acta Mater.* 51, 4471 (2003).
 8. G. Dehm, T. J. Balk, B. von Blanckenhagen, P. Gumbsch, and E. Arzt, *Z. Metallk.* 93, 383 (2002).
 9. B. von Blanckenhagen, P. Gumbsch, and E. Arzt, *Modelling Simulation Mat. Sci. Eng.* 9, 157 (2001).
10. M. Legros, K. J. Hemker, A. Gouldstone, S. Suresh, R.-M. Keller-Flaig, and E. Arzt, *Acta Mater.* 50, 3435 (2002).
11. B. von Blanckenhagen, P. Gumbsch, and E. Arzt. *Philos. Mag. Lett.* 83, 1 (2003).
12. H. Gao, L. Zhang, W. D. Nix, C. V. Thompson, and E. Arzt, *Acta Mater.* 47, 2865 (1999).
13. M. D. Thouless, J. Gupta, and J. M. E. Harper, *J. Mat. Res.* 8, 1845 (1993).
14. J. R. Rice and R. Thomson, *Philos. Mag.* 29, 73 (1974).
15. Z. Suo and J. W. Hutchinson, *Int. J. Solids Struct.* 25, 1337 (1989).
16. J. P. Hirth and J. Lothe, "Theory of Dislocations." Wiley-Interscience, 1982.
17. J. D. Eshelby, in "Dislocations in Solids" (F. R. N. Nabarro, Ed.), Vol. 1, p. 167. North-Holland, Amsterdam, 1979.
18. L. Zhang and H. Gao. *Z. Metallk.* 93, 417 (2002).
19. R. L. Coble, *J. Appl. Phys.* 41, 1679 (1963).

20. F. Ergodan, G. D. Gupta, and T. S. Cook, "Methods of Analysis and Solutions of Crack Problems," pp. 168–425. Nordhoff Leyden, 1973.
21. F. Ergodan and G. D. Gupta, *Q. Appl. Math.* 30, 525 (1972).
22. H. Gao, Y. Huang, W. D. Nix, and J. W. Hutchinson, *J. Mech. Phys. Solids* 47, 1239 (1999).
23. J. R. Rice and T.-J. Chuang, *J. Am. Ceram. Soc.* 64, 46 (1981).
24. W. W. Mullins, *J. Appl. Phys.* 28, 333 (1957).
25. D. Weiss, H. Gao, and E. Arzt, *Acta Mater.* 49, 2395 (2001).
26. Z. C. Xia and J. W. Hutchinson, *J. Mech. Phys. Solids* 48, 1107 (2000).
27. L. Zhang, Ph.D. thesis, Stanford University, 2001.
28. M. J. Buehler, A. Hartmaier, and H. Gao, *J. Mech. Phys. Solids* 51, 2105 (2003).
29. A. R. Zak and M. L. Williams, *J. Appl. Mech.* 30, 142 (1963).
30. M. J. Buehler, A. Hartmaier, and H. Gao, *Model. Sim. Mat. Sci. Eng.* (2003) (unpublished).
31. A. Hartmaier, M. J. Buehler, and H. Gao, "Defects and Diffusion in Metals–Annual Retrospective, Defect and Diffusion Forum."
32. M. J. Buehler, A. Hartmaier, and H. Gao, *Mat. Res. Soc. Symp. Proc.* 779, W4.7.1 (2003).
33. M. J. Buehler and H. Gao, "Handbook of Theoretical and Computational Nanotechnology." American Scientific Publishers, 2004.
34. H. van Swygenhoven, P. M. Derlet, and A. Hasnaoui, *Phys. Rev. B* 66, 024101 (2002).
35. D. Wolf, V. Yamakov, S. R. Phillpot, and A. K. Mukherjee, *Z. Metallk.* 94, 1052 (2003).
36. V. Yamakov, D. Wolf, S. R. Phillpot, and H. Gleiter. *Acta Mater.* 50, 61 (2002).
37. R. W͑urschum, S. Herth, and U. Brossmann, *Adv. Eng. Mat.* 5, 365 (2003).
38. P. Keblinski, D. Wolf, S. R. Phillpot, and H. Gleiter, *Phil. Mag. Lett.* 76, 143 (1997).
39. P. Keblinski, D. Wolf, S. R. Phillpot, and H. Gleiter, *Phil. Mag. Lett.* 79, 2735 (1999).
40. P. Lagarde and M. Biscondi, *Mem. Etud. Sci. Rev. Met.* 71, 121 (1974).
41. E. Budke, C. Herzig, S. Prokofjev, and L. Shvindlerman, *Defect Diffusion Forum* 156, 21 (1998).
42. Y.-L. Shen, *J. Mater. Res.* 18, 2281 (2003).
43. J. R. Rice and G. B. Beltz, *J. Mech. Phys. Solids* 42, 333 (1994).
44. R. Spolenak, N. Tamura, B. Valek, R. S. Celestre, A. A. MacDowell, T. Marieb, H. Fujimoto, W. L. Brown, J. C. Bravman, H. A. Padmore, B. W. Batterman, and J. R. Patel, *Phys. Rev. Lett.* 90, 096102 (2003).
45. T. J. Balk, G. Dehm, and E. Arzt, *Mat. Res. Soc. Symp. Proc.* 673, 2.7.1 (2001).
46. R. Venkatraman and J. C. Bravman. "Separation of film thickness and grain-boundary strengthening efects in Al thin-films on Si."
47. G. Dehm, B. J. Inkson, T. J. Balk, T. Wagner, and E. Arzt, *Mat. Res. Soc. Symp. Proc.* 673, 2.6.1 (2001).
48. M. J. Kobrinsky and C. V. Thompson, *Acta Mater.* 48, 625 (2000).
49. M. J. Kobrinsky, G. Dehm, C. V. Thompson, and E. Arzt, *Acta Mater.* 49, 3597 (2001).
50. H. J. Frost and M. F. Ashby, "Deformation-Mechanism Maps," 1st ed., p. 21. Pergamon Press, Oxford, 1982.